aerospace

MDPI

Project Report

Conceptual Design of Electrically Powered Urban Air Mobility Vehicles for Psychoacoustic Studies †

Stephen Schade [1], Jonas Ludowicy [2], Patrick Ratei [3], Martin Hepperle [4], Arne Stürmer [4], Philipp Schulze [5], Karl-Stéphane Rossignol [6], Stefanie de Graaf [2] and Thomas F. Geyer [5,*]

1 Department of Engine Acoustics, Institute of Propulsion Technology, German Aerospace Center (DLR), Bismarckstraße 101, 10625 Berlin, Germany; stephen.schade@dlr.de
2 Department of Architecture and Integration of Propulsion System, Institute of Electrified Aero Engines, German Aerospace Center (DLR), Lieberoser Str. 13A, 03046 Cottbus, Germany
3 Department of Aviation System Concepts and Assessment, Institute of System Architectures in Aeronautics, German Aerospace Center (DLR), Hein-Saß-Weg 22, 21129 Hamburg, Germany
4 Department of Transport Aircraft, Institute of Aerodynamics and Flow Technology, German Aerospace Center (DLR), Lilienthalplatz 7, 38108 Braunschweig, Germany
5 Department of Environmental Impact and Sensor Technology, Institute of Electrified Aero Engines, German Aerospace Center (DLR), Lieberoser Str. 13A, 03046 Cottbus, Germany
6 Department of Technical Acoustics, Institute of Aerodynamics and Flow Technology, German Aerospace Center (DLR), Lilienthalplatz 7, 38108 Braunschweig, Germany
* Correspondence: thomas.geyer@dlr.de
† This paper is an extended version of our paper "Conceptual design of electrically-powered Urban Air Mobility vehicles for aeroacoustic studies". In Proceedings of the Deutscher Luft- und Raumfahrtkongress (DLRK) 2024, Hamburg, Germany, 30 September–2 October 2024.

Abstract

In order to provide an innovative form of urban air mobility, a new and versatile generation of small, highly automated aircraft is currently being developed. This is made feasible by the development of new technologies such as electrified powertrains, Vertical Take-Off and Landing capabilities and distributed propulsion systems. The operation of these novel aircraft types will generate a new source of air traffic noise. In particular, the perception of noise and the annoyance caused by these aircraft and their distributed propulsion systems are likely to deviate from those of conventional aircraft and will also depend on psychoacoustic effects. Thus, the noise emission and its subjective perception will be key factors for the success of urban air mobility vehicles and their acceptance by society. In order to investigate acoustic effects that enable low-noise aircraft design, a multidisciplinary approach is applied to develop new aircraft concepts for urban air mobility. This approach includes the conceptual design of two vehicles, one vehicle with tilt-rotors and one with tiltable, ducted fans; the sizing of an electric powertrain; the design and manufacturing of a wingtip rotor; and the design and manufacturing of the low-speed ducted fans. This paper presents the design of the two vehicle architectures, including their electric powertrain, as well as the aerodynamic and acoustic performance of the rotor and fan.

Keywords: urban air mobility; distributed electric propulsion; noise perception

Academic Editors: Konstantinos Kontis, Lawrence S. Ukeiley, Lothar Bertsch and Rainer Schmid

Received: 6 October 2025
Revised: 17 March 2026
Accepted: 18 March 2026
Published: 26 March 2026

1. Introduction and State of the Art

1.1. Motivation

In the civil transportation sector, the use of urban air mobility (UAM) vehicles is receiving increased attention, with an emerging variety of different vehicle designs (see, for example, [1–7]). Electrified propulsion systems with distributed, low-speed fan stages

or distributed propellers are being developed for next-generation urban and regional aircraft. The noise emission of the propulsion system is a dominant acoustic source, which may be perceived as annoying. Therefore, a detailed investigation of the acoustic mechanisms as well as psychoacoustic metrics is required, thus enabling a low-noise propulsion system design.

Recent studies have examined a number of innovative propulsion and design concepts for aircraft based on distributed and hybrid approaches. Kim et al. [8] review distributed electric propulsion (DEP) technologies, highlighting their potential to enhance vehicle performance, the robustness of their design and their efficiency. Green et al. [9] provide a conceptual sizing and performance study for an electric distributed propulsion system. Brelje and Martins [10] present a comprehensive overview of propulsion concepts for fixed-wing aircraft with varying degrees of electrification, ranging from fully electric to hybrid and turboelectric systems. Their work considers configuration options, underlying technologies, and design methods, and outlines the technological obstacles impacting the development of future aircraft with electrified propulsion. Researchers from the National Aeronautics and Space Administration (NASA) published a broader series of work investigating vehicle requirements and technology constraints for future UAM vehicles. As part of this series, Johnson et al. [1] and Silva et al. [11,12] provide the conceptual design of several VTOL (Vertical Take-Off and Landing) concept vehicles, Patterson et al. [13] establish a set of UAM sizing mission requirements and Antcliff et al. [14] discuss the technology assumptions made to design the vehicles and identify future research directions for the next generation of UAM vehicles.

1.2. Acoustics of Distributed Electric Propulsion Systems

The noise generated by single open rotors and that by ducted fans are classical problems in aeroacoustics (see, for example, [15–18] and [19–22]). In both cases, the far-field sound pressure spectrum, which consists of tonal and broadband noise contributions, is highly directional.

When the interaction of multiple open rotors or fans with other propulsors and/or with the airframe and other supporting structures is taken into account, the noise radiation becomes even more complex, and additional interaction noise sources may emerge as well. Moreover, propulsion systems with distributed thrust offer new degrees of freedom in terms of design compared to conventional engine configurations, for example, with regard to the number and arrangement of propulsors on an aircraft. For instance, Borer et al. [23] provide the conceptual design of the NASA SCEPTOR flight demonstrator, for which an existing aircraft is reconfigured with a distributed propulsion system through multiple leading-edge propellers and larger wingtip cruise propellers. With regard to the aerodynamic design, the authors conclude that this design approach enables a reduction in wing area and drag with maintained performance at low speeds, illustrating how distributed propulsion can provide aerodynamic improvements in electric aircraft. With regard to acoustics, new degrees of freedom may represent an opportunity to reduce noise emissions in the future. However, new degrees of freedom may also change the aural impression of these distributed electric propulsion systems compared to conventional concepts. Reasons for this difference are acoustic interaction, modulation and interference effects mainly resulting from the number and installation of the propulsors (see, for example, [24–26]). Due to these effects, the noise perception by human observers and the subsequent annoyance may also be different compared to common small aircraft. In addition, psychoacoustic measures, such as loudness, sharpness, tonality, roughness and impulsiveness, are prone to be affected by distributed electric propulsion systems, e.g., due to variations in rotational speed of single propulsors, interference effects, shielding, interaction noise sources and the

additional high-frequency tonal noise contribution from high-power, fast-running electric motors [27]. Thus, noise perception will be a key factor regarding the public acceptance of these aircraft concepts [28].

One prototype UAM vehicle for which acoustic data are available is the Joby aircraft, an eVTOL (electric Vertical Take-Off and Landing) aircraft driven by six tiltable five-bladed open rotors. In [29], detailed microphone arrays are described, which are used to obtain noise contours of departures and approaches of the Joby prototype vehicle. The results were used for comparison with high-fidelity computations of flyover noise [30] as well as approach and departure noise [31], showing reasonable agreement. More recently, detailed acoustic wind tunnel measurements on the propellers of the Joby aircraft were performed [32], providing a database for further validation of noise prediction tools.

1.3. State-of-the-Art Noise Prediction and Acoustic Assessment

Past research has already focused on the prediction of aircraft noise by evaluating the generation and radiation of noise in the early phases of conceptual design. In the investigation by Iemma and Diez [33], models for the prediction of airframe noise were included in an optimization routine for aircraft conceptual design, although noise from the propulsion system was not considered. The flyover noise from the hybrid wing–body aircraft design HWB C11 by NASA was predicted and compared to that of a reference tube-and-wing aircraft by Rizzi et al. [34] using the NASA Aircraft Noise Prediction Program (ANOPP). The results are audio and visual representations that can be used in further studies to determine psychoacoustic metrics. This methodology was further illustrated in [35] using four different case studies, showing that it is indeed possible to evaluate human perception to aircraft noise during the design process. This methodology was also applied to the SCEPTOR aircraft design with a distributed electric propulsion system as mentioned above [36], which includes the prediction of propeller noise performed with the PSU-WOPWOP code [37]. Through psychoacoustic tests on 32 subjects, it was observed that annoyance varies significantly with the number of propulsors and with time-varying effects such as atmospheric turbulence but not with differences in rotational speed between propellers. Another methodology to predict aircraft noise annoyance metrics as part of the aircraft design was published by Sahai et al. [38]. It is based on the Integrated Noise Simulation and Assessment module (INSTANT) [39] and allows for the calculation of physical (certification-related) noise metrics, such as the effective perceived noise level (EPNL), as well as perception-based metrics. Another tool for the prediction of aircraft flyover noise is sonAIR [40], developed by the Swiss Federal Laboratories for Materials Testing and Research (EMPA). It allows the calculation of physical noise metrics, including noise maps. The program was also extended to the prediction of noise from multicopters [41], wherein the modeling of the rotor noise emission was based on measurements. At the German Aerospace Center (DLR), the tools PANAM (Parametric Aircraft Noise Analysis Module) [42] and PropNoise (PropulsionNoise) [43] were developed for the prediction of total aircraft noise and propulsion system noise during the conceptual design phase, respectively. Recently, PANAM was integrated into a routine for the perception-based noise assessment of a future blended wing body aircraft concept with geared turbofan engines [44]. With the aim of simulating and auralizing the sound emitted by aircraft propulsion systems, PropNoise was recently integrated into a framework [45] together with the tools VIOLIN (virtual acoustic flyover simulation) and CORAL (aircraft engine noise auralization), allowing for virtual flyover simulation and binaural noise synthesis [45]. Initial studies were conducted using this framework to evaluate the influence of fan design [46] and impact of rotational speed variations [47] on the psychoacoustic characteristics of a distributed propulsion system.

A more general review of state-of-the-art methods for aircraft noise prediction, simulation and minimization is given in [48], while a comparison of three different aircraft noise prediction programs can be found in [49].

1.4. The VIRLWINT Project

In a current research project of the German Aerospace Center called VIRLWINT, two different eVTOL vehicle concepts have been designed with the aim of enabling detailed investigations of the noise emission and noise perception caused by different distributed electric propulsion systems. One design is based on the use of eight distributed open rotors, while the second vehicle is powered by 26 distributed ducted fans. Based on these vehicle designs, an experimental acoustic investigation of the propulsion systems will be performed in the next step of the project based on predictions of sound radiation calculated on the basis of detailed acoustic measurements on individual propulsors as well as a representative electric machine. Thus, the project's approach described in the current report is basically similar to some of the previous studies [36,50]. However, it should be emphasized that the focus of the VIRLWINT project is on the perceived noise from two UAM concept vehicles with distinctly different propulsion systems, which, to the authors' best knowledge, has not been investigated before.

Typically, the acoustic design process relies on the evaluation of single noise metrics, such as the sound pressure level or the EPNL. These metrics reduce complex noise exposure to a single value. The design with the lowest value, e.g., the lowest EPNL, is usually chosen. However, EPNL, although relevant for noise certification, may not capture psychoacoustic characteristics and hence human perception. Consequently, the minimum-EPNL design is not always the least annoying [35,51]. This issue is especially important for distributed electric propulsion systems, whose noise signatures differ from those of conventional aircraft [28,52]. A solution is to link acoustic design with listening tests involving human subjects. In this loop, synthesized audio files serve as stimuli, and the resulting subjective ratings then guide the design process. This approach is known as perception-informed design [35]. Auralization enables perception-informed design by converting analytical, numerical, or experimental data such as time-dependent sound pressure levels from virtual flyovers into audio files. These files can then be used in listening experiments [53–55]. Thus, auralization bridges metrics-driven and perception-influenced design, making the engine and vehicle noise signatures both quantifiable and perceptible. A detailed comparison of two auralization methods is given in [56], which even mentions the necessity of annoyance models for the design of UAM vehicles. The VIRLWINT project advances this pathway by developing a measurement-informed auralization framework to provide highly accurate auralization data of distributed electric propulsion systems. This measurement-informed auralization framework is an extension of the above-mentioned analytical framework based on PropNoise, VIOLIN and CORAL. Therefore, high-precision measurements of representative propulsors, taken in a fan test facility and an aeroacoustic wind tunnel, and measurements of a representative electric machine are combined with the virtual flyover (VIOLIN) and binaural noise synthesis (CORAL) framework. This yields noise signatures for different distributed electric propulsion systems. The resulting audio files will then be used in listening tests with human subjects in a later phase of the VIRLWINT project. In order to enable these psychoacoustic studies, a conceptual design of two electrically powered UAM vehicles, including their powertrains and propulsion systems, was performed.

1.5. Outline of This Report

This report outlines the conceptual UAM vehicle design as well as the design of the open propellers, ducted fans and the electric powertrain, all having a major influence on aircraft mass, performance and noise. However, it should be noted that psychoacoustic analyses will be performed at a later stage of the VIRLWINT project and are thus not covered in the present report. The basic procedure of this work is outlined in Figure 1. Thus, the present report is meant to serve as an overview of the technical disciplines that are involved in the design of such concept vehicles. It is organized as follows: The Top-Level Aircraft Requirements (TLARs) are detailed in Section 2. The conceptual design of the two vehicles is detailed in Section 3 and that of the electric powertrain in Section 4. Section 5 then describes the design of an example electric machine, Section 6 handles the propeller design and Section 7 describes the design of the ducted fans. Finally, Section 8 summarizes the main findings and provides an outlook for future studies.

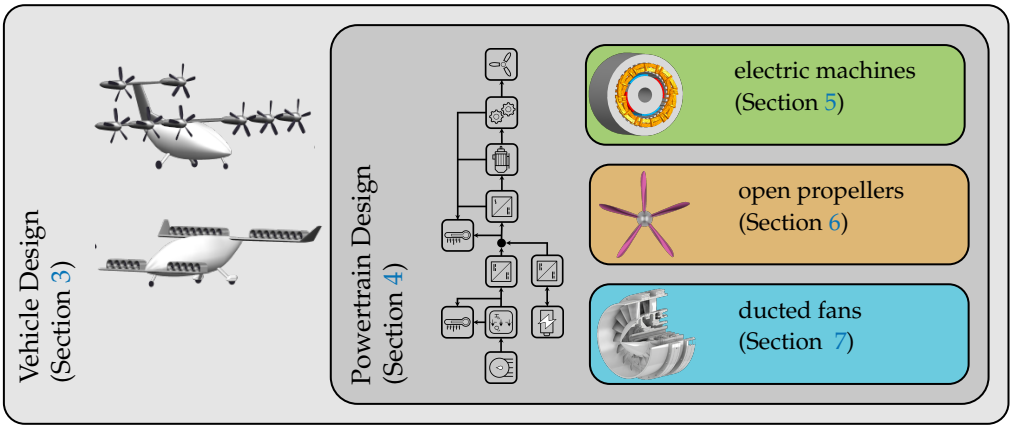

Figure 1. Overview of the basic content of the present study.

2. Top-Level Aircraft Requirements and Initial Powertrain Considerations

The initial Top-Level Aircraft Requirements are identical for both vehicle concepts and should reflect the use case of an intercity urban passenger transport. They were derived from previous results of the HorizonUAM project [57], in which a wide range of UAM use cases and their corresponding vehicle requirements were proposed. The most relevant parameters are summarized in Table 1, while additional considerations are discussed in the following. The corresponding altitude and velocity of the selected mission are shown in Figure 2. Potential use cases demand vehicles with VTOL capability for brief hover times of less than 30 s. The aircraft must comply with EASA's special condition for VTOL, which limits the Maximum Take-Off Mass (MTOM) to less than 3175 kg. The design must ensure continued safe flight and vertical landing in any failure scenario. Further requirements, aligned with Uber Elevate, dictate that infrastructure constraints be met, limiting the overall dimensions to 15.3 m × 15.3 m × 6.1 m (length × width × height). Moreover, taxiing during ground operations must be possible without external devices, requiring the vehicle to maneuver independently of ground support equipment. Finally, the avionics systems shall support highly automated flight operations, even though initial UAM applications may involve piloted vehicles.

Table 1. Initial Top-Level Aircraft Requirements for both vehicle designs.

Range	100 km (plus 20 min reserve)
Flight speed	200–250 km/h
MTOM	<3175 kg
Payload	450 kg (1 pilot + 4 passengers)
EIS	2030–2035

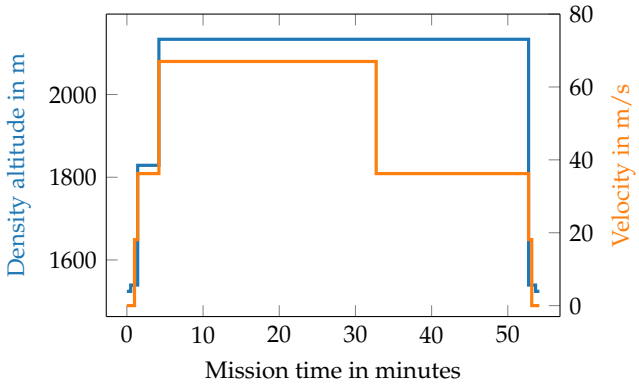

Figure 2. Altitude and velocity mission profile used for both vehicles.

On the overall propulsion system level, two different propulsion units, i.e., open rotors and ducted fans, are planned for the design in order to analyze and assess them in acoustic studies at a later point. Regarding the design of the electric powertrain, three different topologies are being considered: one is a fully battery-electric propulsion system, the second is a propulsion system powered solely by fuel cells and the third is a hybrid system with varying degrees of hybridization.

3. Conceptual Vehicle

3.1. Method

Based on the initial TLARs, the conceptual vehicle design process is initiated to derive the overall vehicle specifications, including basic geometry and performance parameters. The design and sizing methodology employed in this work is based on established handbook techniques derived from Class II methods in conceptual aircraft and rotorcraft design. Special emphasis is placed on methods suitable for unconventional vehicle configurations within UAM applications. This methodology was first applied and integrated into a broader simulation framework for vehicle and fleet-level design in the work presented in [58,59], and is documented in full detail in [60].

The design and assessment of novel vehicle concepts requires the integration of multiple disciplines. It begins with the initial sizing and concept development of the vehicle architecture, including powertrain sizing, and extends to the detailed design of the propulsors, which are a key focus of this project for subsequent comparative noise assessments. This results in an iterative, multidisciplinary workflow spanning all the disciplines outlined in the following sections. Their interactions, along with high-level data and information exchange throughout the design process, are illustrated in Figure 3. As part of the conceptual design phase, an initial vehicle was developed using the baseline parameters of the conceptual design tool. The initial results, including mission and point performance characteristics of the vehicle (e.g., aerodynamic coefficients and propulsive power), were used as a baseline for the detailed design disciplines discussed in the subsequent chapters. Subsequently, the outputs of the detailed design disciplines (e.g., propulsion system performance and powertrain masses) were integrated back into the overall vehicle model to further refine the vehicle concepts.

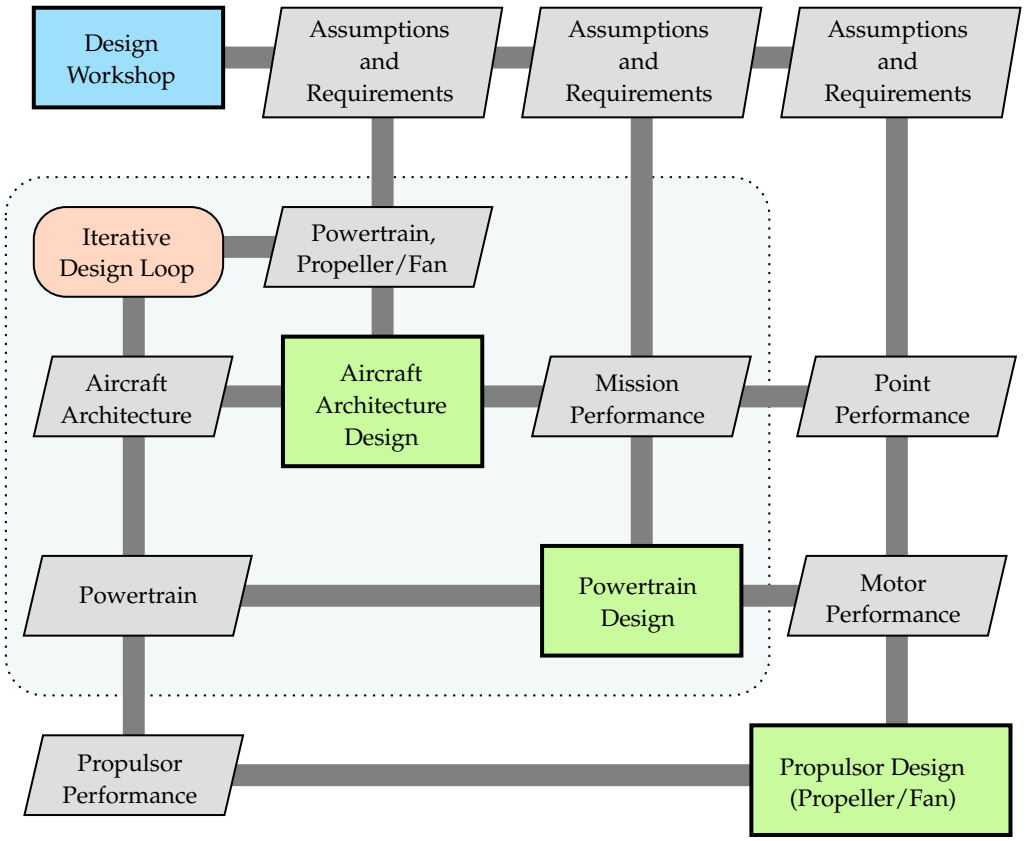

Figure 3. Schematic overview of the multidisciplinary vehicle design workflow as organized in the extended design structure matrix.

Figure 4 provides an overview of the methodological building blocks used for the initial sizing and overall aircraft design of the two vehicle architectures. The process starts with mission parameters and geometrical considerations of the fuselage, wing and propulsor as primary inputs. Based on these inputs, an initial sizing of the wing and propulsor is performed, including the estimation of their performance characteristics. Subsequently, the component masses are estimated and iterated until convergence of the MTOM is achieved. The implementation and application of this tool were validated against other research in the field of UAM vehicle design, showing good agreement (see the validation presented in [60]). Consequently, the tool was employed for the design of these novel vehicle concepts within the context of this work. The initial sizing results were then iteratively updated based on domain-level sizing results (e.g., powertrain, propeller, or ducted fan as illustrated in Figure 3) to enable comprehensive overall aircraft design and mission performance analysis.

3.2. Results

Following sensitivity studies of the initial TLARs and qualitatively comparative studies of the architectural and configurational vehicle design options, the design space was narrowed down step by step. Based on sensitivity studies for both vehicle concepts, the design range and cruise speed were found to be highly sensitive to the sizing of the battery-electric powertrain. As a result, the optimal design point was identified with a range of 100 km and a cruise speed of 200 km/h. It is important to note that this design range does not account for reserves; however, an additional 20 min of loiter time—nearly half of the operational-flight duration—is included. The operational range may eventually be extended by accounting for the required reserves during flight planning for the actual transport network.

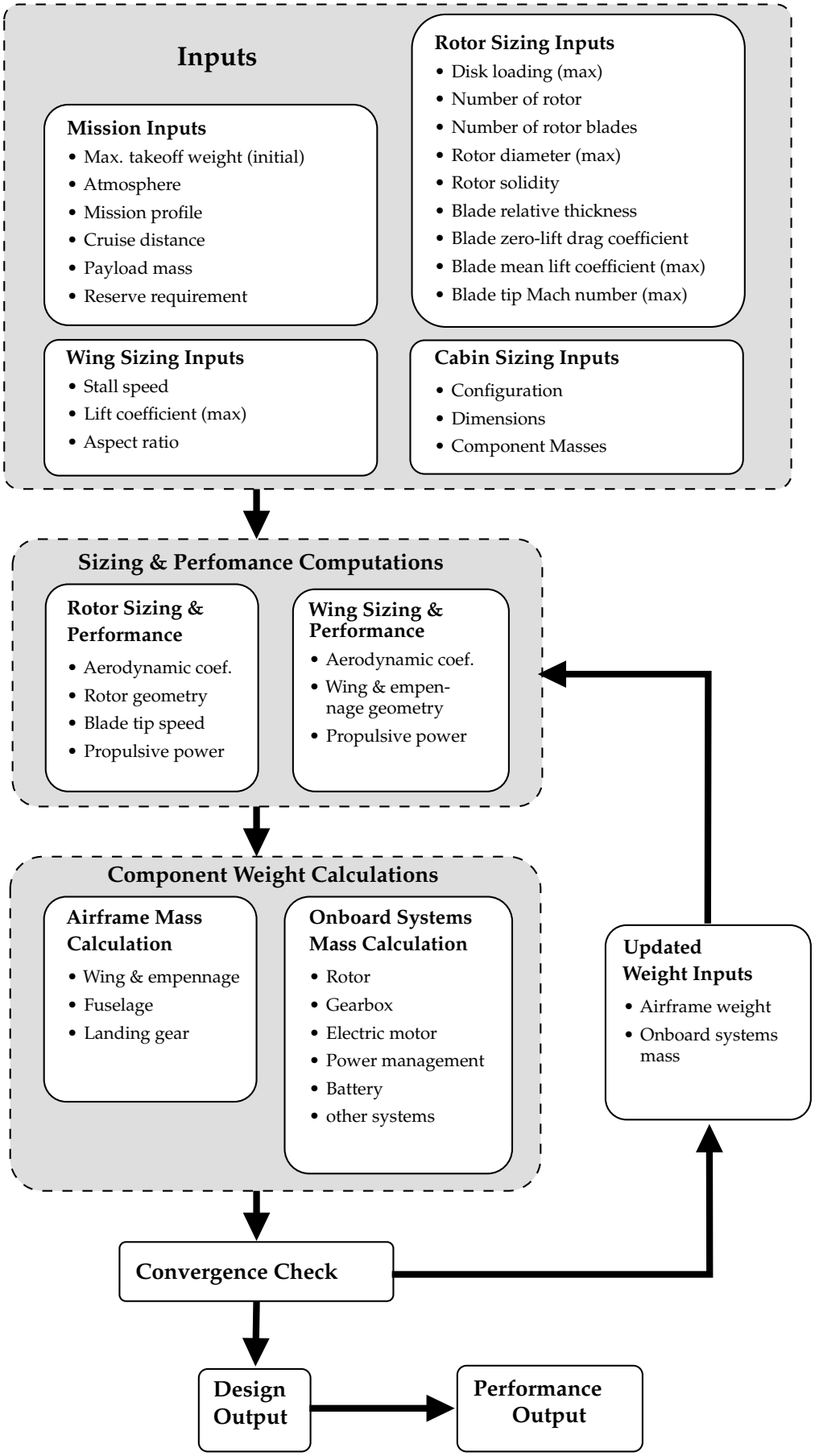

Figure 4. Methodology and iterative process for initial sizing and vehicle architecture design (reproduced from [60]).

Finally, the iterative conceptual vehicle design process resulted in two concepts that represent a preliminary design output, which will be finalized as soon as all higher-fidelity simulations and assessments are fed back to the overall vehicle design loop at a later stage. Figures 5 and 6 display the resulting 3D models of both vehicle concepts (note that the two figures are not shown to the exact same scale). The specifications, including basic geometry and performance parameters, can be found in Table 2.

(**a**) Isometric view. (**b**) Side view.

Figure 5. 3D model of the tilt-rotor vehicle concept showing the integration of the open rotors, with overall dimensions 7.7 m × 13.9 m × 5.1 m (length × width × height).

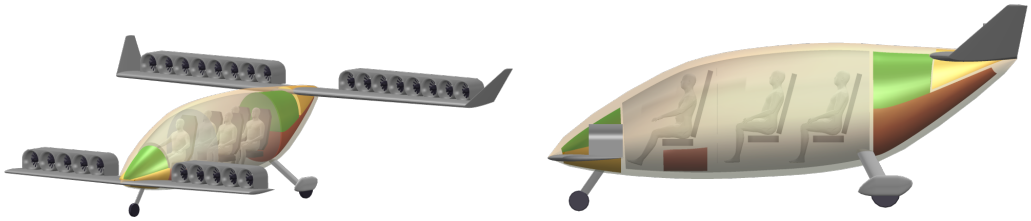

(**a**) Isometric view. (**b**) Side view.

Figure 6. 3D model of the tilt-duct vehicle concept showing the integration of the ducted fans, with overall dimensions 7 m × 11.7 m × 3 m (length × width × height).

Table 2. Vehicle specifications.

	Tilt-Rotor	**Tilt-Duct**
MTOM, kg	2334	2927
Payload mass, kg	450	450
Airframe mass, kg	676	677
Powertrain mass, kg	1019	1600
Systems mass, kg	189	200
Disc loading, $N\,m^{-2}$	1065	6645
Number of disks	8	26
Disc diameter, m	1.85	0.46
Wing area, m^2	12	12.6
Wing span, m	12	11.7
Canard area, m^2	–	7
Canard span, m	–	7
Hover power, kW	896	1259
Cruise power, kW	105	156
Cruise lift-to-drag ratio	12.1	10.2

While each vehicle concept could be further optimized by adjusting the TLARs, leading to two distinct optimal solutions, the focus here was to design both concepts for the same design point. This approach was chosen to allow for better comparison in the acoustic studies and, at the same time, to design generally representative UAM vehicle concepts.

Initial higher-fidelity RANS (Reynolds-Averaged Navier Stokes equation)-based studies of the tilt-rotor vehicle concept were performed using the DLR TAU-Code [61,62]. The main goal of these simulations was to refine the aerodynamic design of the vehicle to a degree which enables the derivation of a representative wind tunnel model, which is intended to be used to provide input data for the auralization of a tip-mounted-propeller configuration. Additionally, the RANS results will be used to guide a possible future refinement of the tilt-rotor vehicle as well as to support the development and improvement of the tools, approaches and assumptions used in the conceptual vehicle design.

Utilizing a semi-automated process chain comprising a parametric CAD model, the mesh generation process and the TAU CFD simulation, the wing and horizontal tailplane twist was iterated at four and two spanwise stations, respectively, with the aim of achieving the required overall aircraft lift for trimmed flight at the cruise operating point. Based on the specifications and the geometrical output of the conceptual design, the main modifications introduced in the CAD model used for the RANS studies were the omission of the landing gear to simplify the mesh generation process, the introduction of a dorsal fairing to allow for an aerodynamically clean intersection of the wing and fuselage and the modification of the specified baseline airfoils to obtain realistically sized thick trailing edges.

A view of the aerodynamically refined configuration as iteratively developed in these high-fidelity studies can be seen in Figure 7, which shows a result of the RANS simulation, plotting contours of vorticity to highlight the development of wakes and vortices around the aircraft.

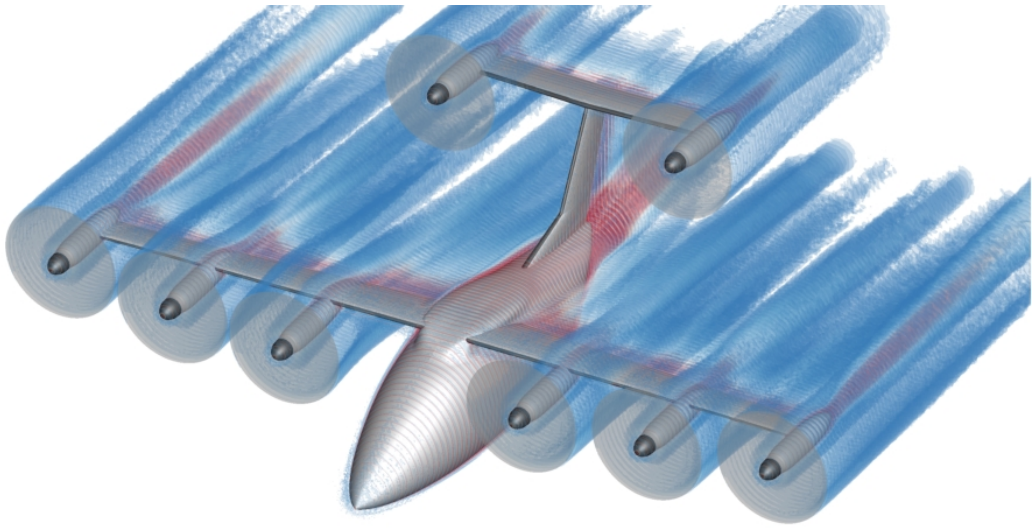

Figure 7. RANS simulation result of the aerodynamically refined tilt-rotor at cruise conditions.

Also evident in Figure 7 is the use of the actuator disc propeller model in the TAU-RANS simulations to ensure that propeller slipstream and power effects on the vehicle are captured and accounted for in this aerodynamic analysis.

The final iteration in the RANS-based study, a vehicle that achieves the required lift for trimmed flight at the cruise operating point, was found to show a notably higher efficiency than determined in the conceptual design. The lower drag of the airframe found in the CFD analysis is partially due to the omission of the landing gear but also indicates that some overly conservative estimates on component drag values were likely assumed in the conceptual design. Thus, it is quite possible that there is significant potential to further optimize the tilt-rotor vehicle and/or the mission specifications in possible follow-up investigations.

Another iteration of the RANS-based aerodynamic design refinement is planned, as the specified baseline airfoils were found to result in a wing thickness at the intersection with the wingtip propeller nacelle that will be unsuitably thin in the planned model scale to accommodate all the required instrumentation. Finally, a verification of the hover performance of the air vehicle is planned to ensure that this operating point is also comfortably achievable with the baseline configuration developed in the conceptual design.

4. Powertrain

4.1. Method

For both of these vehicle concepts, different powertrain topologies are analyzed by means of preliminary sizing results. The three powertrain topologies (battery, fuel cell and hybrid system) are each sized for the respective vehicle requirements. An overview of the topologies and the components represented within is shown in Figure 8. All powertrains have the left side in common, starting with the mechanical shaft power from the propeller via an optional gearbox over an electric motor and inverter to direct current (DC) electric power. This part, called the electric drivetrain (EDT), has a dedicated active thermal management system (TMS) for its components. Depending on the type of powertrain, the DC electric power is preconditioned to the system-level voltage and supplied by either batteries, a fuel cell system (FCS), or a combination of both in the hybrid variant.

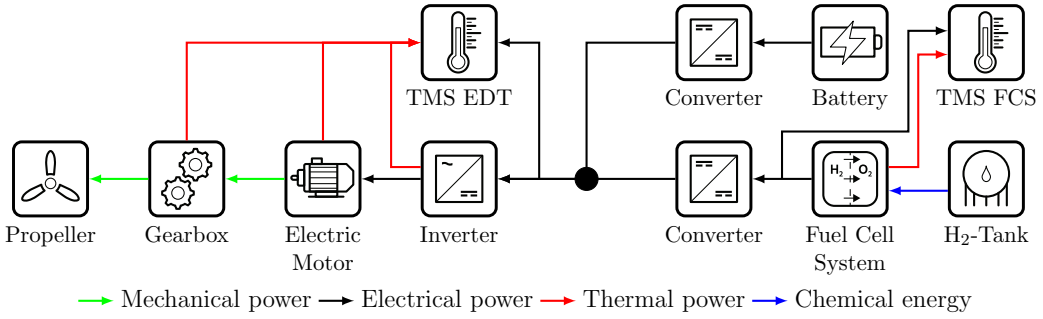

Figure 8. Overview of powertrain topologies and components.

An in-house tool is used for the preliminary sizing of the powertrain components in terms of performance, mass and volume. The individual components are modeled for their performance as described by Staggat et al. [63] and Ludowicy et al. [64]. An empirical model is used for the gearbox, while the motor and inverter use analytical models which assume a permanent magnet synchronous motor and a three-level neutral-point-clamped architecture for the inverter. Based on polarization curves from existing proton-exchange membrane fuel cells, with the addition of simple analytical descriptions of the necessary balance of plant components, the fuel cell system is modeled semi-empirically. To calculate masses, the power-to-weight ratios or energy densities listed in Table 3 are used to account for technology projections. Exceptions are the TMS and the hydrogen tank. For the TMS, the components within (heat exchanger, pipes, pumps, fluids, fans) are sized based on a mix of empirical and analytical models. The whole TMS design process was described in more detail by Link and Staggat [65]. Bahrs et al. [66] described the sizing of the hydrogen tanks using analytical models for the different storage options, which include gaseous storage tanks at different pressure levels, different metal hydride storage systems and a cryogenic storage tank.

Table 3. Powertrain mass estimation values.

Component	Mass Estimation Value
Electric motors	13.2 kW/kg
Power electronics	13.8 kW/kg
Fuel cell system	6 kW/kg
Batteries	391 Wh/kg

The sizing of the components is based on the shaft power requirements over the course of the whole mission, which is shown in Figure 9. For the EDT components, the design point is simply the maximum shaft power output during the mission with the environmental conditions in the corresponding flight phase. The FCS is sized either for the same design point to solely deliver the electric power to the EDT or, in the case where the powertrain is a hybrid system, by the hybridization factor

$$H_P = \frac{P_{\text{electric design FCS}}}{P_{\text{electric design EDT}}}, \tag{1}$$

whereby its design power is put in relation to the electric power for the EDT in the design point. The definition allows battery-only powertrains ($H_P = 0$), all combinations of hybrids utilizing battery and fuel cell systems to different degrees ($0 < H_P < 1$) and fuel-cell-only options ($H_P = 1$). After the design of these systems, in the mission simulation, the fuel cell system is always utilized first and the battery only used when necessary. This hybridization strategy can be described as peak power shaving.

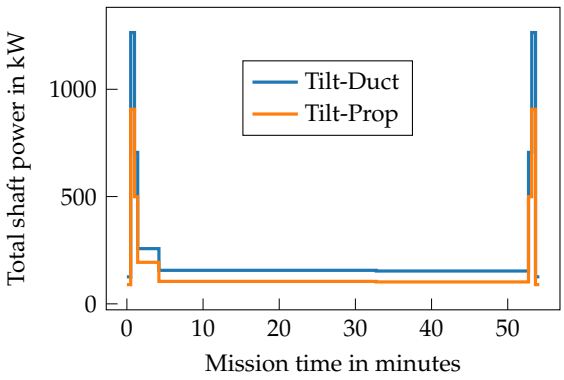

Figure 9. Power profiles for both vehicles.

The battery and the hydrogen tank are sized after the entire mission is simulated with the sized components using discrete time steps. For the hydrogen tank, the consumed hydrogen masses of each mission time step are summed, and different storage options are analyzed, of which the lightest is chosen. For the battery sizing, the actual power drawn in each time step is used, and cells are added to the battery in parallel or series until the required overall energy, power in each time step and voltage requirements are fulfilled by the battery pack. Based on the nominal capacity of this battery, the mass is calculated using the battery gravimetric energy density to enable technology projections. The battery sizing algorithm is described in more detail in Ludowicy et al. [64]. One major change was made to the model, where the underlying cell curves of the single battery cell behavior were exchanged for curves representing a higher-power cylindrical 4680 battery cell used in electric cars [67]. A comparison of the maximum discharge c-rates of both cells is depicted in Figure 10. The standard higher-energy cell that was previously used proved not to be the ideal cell type for these powertrains, as the batteries had to be significantly oversized to ensure that the required power could be drawn over the course of the missions.

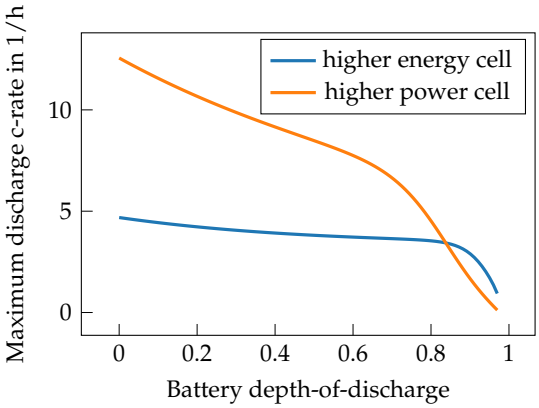

Figure 10. Battery cell comparison.

An iterative process between the propulsion system and vehicle design should be employed to converge on the final configurations of the tilt-rotor and tilt-duct vehicles.

4.2. Results

The powertrain configuration significantly impacts total vehicle mass and therefore noise generation. The presented vehicle designs are only valid with the powertrain masses listed in Table 2. With different powertrain topology and powertrain inputs, the total powertrain mass varies, but those results are not iteratively fed back to the vehicle design; all powertrain results are based on the previously presented vehicle designs and their requirements. A new iteration between vehicle and powertrain design would have to be carried out until convergence to get absolute results on powertrain masses.

Exemplary results for battery-only powertrains for both vehicle concepts are shown in Table 4. The battery-only powertrain for the tilt-rotor vehicle in this interim calculation weighs 1196 kg. The largest share, as was expected, belongs to the batteries, with 570 kg or nearly 48%. The second largest contributor is the electric motors, with 237 kg or 19.8%, followed by the tilt mechanism, the power electronics and the propulsor itself as well as the TMS. The powertrain is 1196 kg heavier than the assumed 1019 kg from the vehicle design; hence, the vehicle could not be built as is. Further studies presented in Ludowicy et al. [67] showed that a design with a hybrid powertrain would be possible and would even exceed the requirements.

Table 4. Battery powertrain mass breakdown.

	Masses in kg	
	Tilt-Rotor	**Tilt-Duct**
Propulsors	30.23	42.15
Tilt Mechanisms	154.25	215.05
E-Motors	237.06	118.65
Inverters	99.37	104.36
TMS EDT	30.35	54.29
Converter Batteries	74.45	107.42
Batteries	570.59	937.77
Total	1196.30	1580.06

From the mission data shown in Figure 9, it is already clear that the tilt-duct vehicle has higher maximum power requirements over the mission than the tilt-rotor vehicle, and hence a higher powertrain mass is to be expected and assumed, at 1600 kg. The battery-only powertrain for the tilt-duct vehicle in this calculation weighs about 1580 kg; hence, the vehicle is a valid design. Again, the batteries comprise the largest share, this time with

nearly 60% of the total mass. For this powertrain, the electric motors are not as heavy and are lighter than for the tilt-rotor vehicle, with only 118 kg or 7.4% of the whole powertrain. The reason is the difference in the rotational speeds of the propulsors, as the ducted fans run at a faster rotational speed than the propellers. Higher rotational speeds allow for lighter motor designs with lower torque and, therefore, lower current and mass.

Figure 11 shows the state of charge and battery cell voltage over the course of the mission for the tilt-rotor vehicle powertrain. It can be seen that in this case, the batteries are not fully discharged over the course of the mission to the 20% deep discharge protection level. Instead, they retain about 30% of their nominal capacity and are therefore oversized from an energy-only perspective. The reason is the battery load profile and its impact on battery cell voltage. The cell voltage drop to just over 2.5 V (the lower voltage limit) at the end of the mission is congruent to the peak in power in the mission profile in Figure 9 for the vertical landing. It is essential for the battery size to still be able to deliver the requested power at the corresponding state of charge, yielding an energy-oversized battery. A battery model purely focused on energy content would therefore underestimate the battery mass. These results emphasize the importance of a suitable battery model to be able to capture these effects.

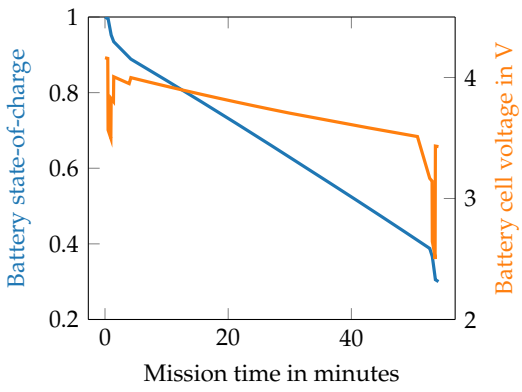

Figure 11. Tilt-rotor battery results.

Gearboxes with different transmission ratios were also analyzed for both vehicles, and the results for the tilt-duct battery powertrain are depicted in Figure 12. There is a mass optimal gearbox transmission ratio of about 0.5 which results in double the motor rotational speed and hence lighter motors. The motor mass is reduced by about 40%, but the additional mass of the gearbox plus further mass penalties due to a decreased efficiency of the powertrain increase the total mass again. Therefore the minimum mass of a powertrain including a gearbox is, in this scenario, 1582 kg, slightly higher than the variant without a gearbox and 1580 kg of total mass as listed in Table 4.

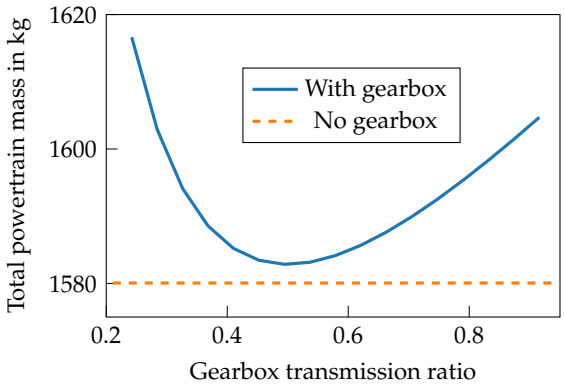

Figure 12. Tilt-duct gearbox study.

In addition to the battery-only powertrain, hybrid powertrains comprising batteries and an FCS were analyzed for both vehicles, as presented in Figure 8. The results for the tilt-duct vehicle are shown in Figure 13. For hybridization factors between 0.1 and 0.45, the overall powertrain mass of the hybrids is lighter than the battery-only variant. The mass minimum is found at about 0.19, with only 1508 kg of total powertrain mass. This configuration has a fuel cell system sized to slightly above the electric power demand during cruise; hence, during cruise, no power from the batteries is necessary. This way, the advantages of both energy systems can be combined, that is, the high gravimetric energy density of hydrogen without the need for a powerful and heavy FCS, while the batteries can be significantly downsized in comparison to the battery-only configuration, as they only have to store energy for the high-power phases where they act as boosters.

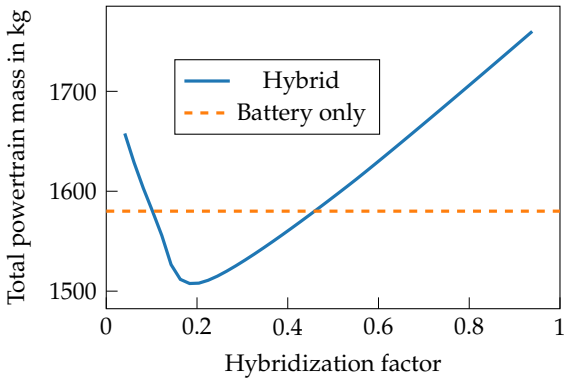

Figure 13. Tilt-duct hybridization study.

In summary, hybrid electric powertrains with FCS and battery were the lightest option for both vehicles when the FCS was sized to be slightly over cruise power. A gearbox was only beneficial for the slower rotating tilt-prop vehicle, and an advanced battery model proved valuable to capture battery discharge restriction effects. The powertrain with its significant share in overall aircraft mass has a strong influence on overall vehicle size. A detailed analysis of the powertrain therefore enables a detailed aircraft design, which is then used as a strong basis for the noise analysis of such vehicles.

5. Electric Motor

5.1. Method

Starting from the initial sizing calculations presented in Section 4, more detailed models of the electric motors are built to analyze their acoustic behavior. The powertrain sizing tool gives the required electric power as well as the required torque. In addition, the design of the propellers (see Section 6) and that of the ducted fans (Section 7) provides the necessary rotational speed for the propulsors of the tilt-rotor vehicle and those of the tilt-duct vehicle, respectively, to deliver the desired thrust in the hover phase and the cruise phase of the flight mission. Based on this data, approximate designs of the electric motors for acoustic analysis are developed using an open-source design tool for electric machines [68]. The methodology of the motor design and the subsequent electromagnetic and acoustic analyses are outlined in Figure 14.

In general, different topologies of electric machines can potentially provide the desired operational parameters. As radial-flux permanent magnet synchronous machines (PMSMs) are known for their high power density, high efficiency and robustness [69], it was decided to use this topology for the current study. In addition to the required operational parameters such as the rotational speed, some topological and dimensional constraints are required in order to obtain motor designs that are feasible for use in the two vehicle types. This could

be a limitation of the motor size or its mass. It has to be noted, though, that the chosen motor design method provides designs based on standard state-of-the-art technologies. As the sizing of the full electric powertrain described above and detailed in [63,64] is at least partially based on technology projections, the motors obtained with the current methodology will most likely not have the required power density. However, for the intended purpose of numerical simulations of the noise radiated by the electric machines, the chosen approach can still provide important insights.

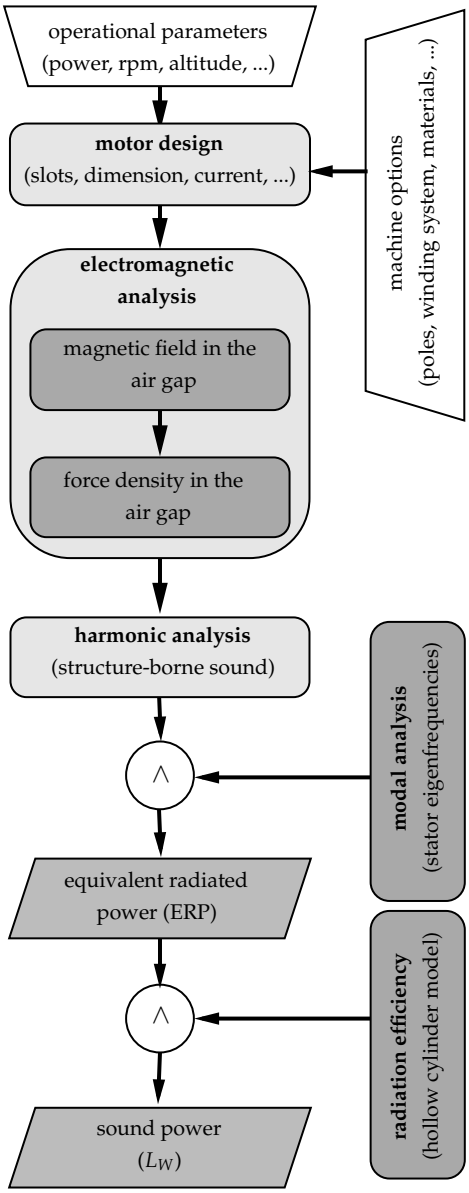

Figure 14. Selected method for the design of electric motors and the calculation of their sound power (motor design according to [68]).

As illustrated in Figure 14, in the next step, the electromagnetic field in the air gap and the resulting radial forces acting on the stator are calculated, which is done using commercial Finite Element Method (FEM) software. In addition to the forces acting on the stator, the noise radiation depends on the eigenfrequencies of the stator, which can be derived analytically or numerically. These calculations yield the so-called equivalent radiated power (ERP). The noise that is effectively propagated into the acoustic far field further depends on the radiation efficiency of the stator, commonly estimated for a simplified

geometry such as a hollow cylinder. It has to be noted that these numerical and analytical calculations are based on simplifying assumptions, such as the neglect of saturation effects, of mechanical coupling effects and others. In addition, the exact mounting of the electric machine in the nacelle as well as additional components connected to the shaft, such as a gearbox, will notably affect the noise radiation.

5.2. Results

For both vehicles, the method for the design of the electric motor outlined above yields a large number of possible electric machines that meet the basic requirements regarding rotational speed and torque. However, some further constraints are necessary in order to obtain feasible results that could potentially meet the additional requirements necessary for their use in eVTOL vehicles. One set of such additional requirements relates to the dimensions of the motor, mainly the outer diameter and the lamination length of the stator, as the available installation space is limited and the weight of the propulsors can be assumed to also scale with the motor size. Another requirement is the current density in the windings of the stator. Although it is known that high current densities potentially enable high power-to-weight ratios, they may also necessitate a liquid cooling system. In the context of UAM vehicles with a large number of propulsors, it may be one design goal to minimize the need for such cooling systems. Other constraints are the number of stator slots, which should not be too large in order to prevent very intricate geometries and to ensure a high winding factor; the number of windings per stator slot; and the upper limits for the electrical frequency and for the saturation levels in the stator and rotor geometry.

As the hover phase of the flight determines the maximum requirements regarding power and torque, these values were used as input for the design of the electric machine. As seen in Table 2, the required continuous power of one such motor for the tilt-duct vehicle is approximately 49 kW. One example design of such an electric machine is shown in Figure 15. This particular motor has a rated power of 49 kW, a rated speed of 8540 rpm and a rated torque of 54 Nm.

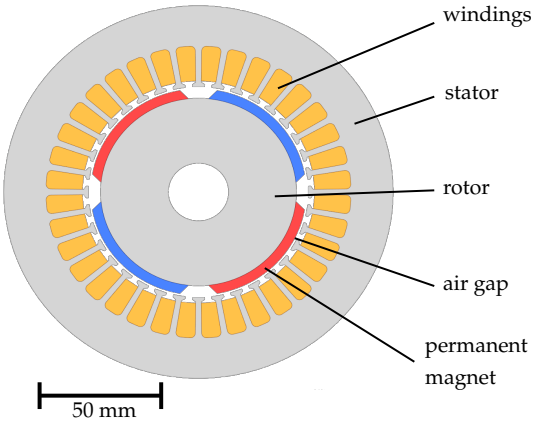

Figure 15. Design of an example PMSM that could be used to power the tilt-rotor vehicle.

However, due to limitations of the motor design tool, it is possible to obtain machine designs that do not result in the desired torque when analyzed with FEM software. For the selected motor design shown in Figure 15, a current density of 16 A/mm^2 is necessary in order to achieve the desired power settings. It remains to be investigated if passive air cooling is still possible or if liquid cooling is required. The permanent magnet on the rotor has two pole pairs, and the stator has 36 slots with eight strands of five windings per slot. With an outer diameter of about 0.21 m and a length of 0.1 m, this is one of the smaller electric machines and hence more suitable for use in the designed tilt-duct vehicle.

Figure 16 shows the radial component of the force density of the example electric machine shown in Figure 15 at the selected operating point corresponding to the hover phase of the flight (rated torque of 54.79 Nm, rated power 49 kW at a rotational speed of 8540 rpm) as a function of the mechanical angle (note that for reasons of symmetry, only one half of the angular range is shown). It is clear that two large radial force fluctuations appear within the shown range of angles, corresponding to the two poles passing the stator surface. These arise from the fundamental magnetic forces generated by the alternating polarity of the rotor poles. Superimposed on these are approximately eighteen smaller ripples caused by slot harmonics from the 36 stator slots. These ripples are caused by the slot openings creating local distortions in the magnetic flux density, leading to higher-frequency radial force fluctuations.

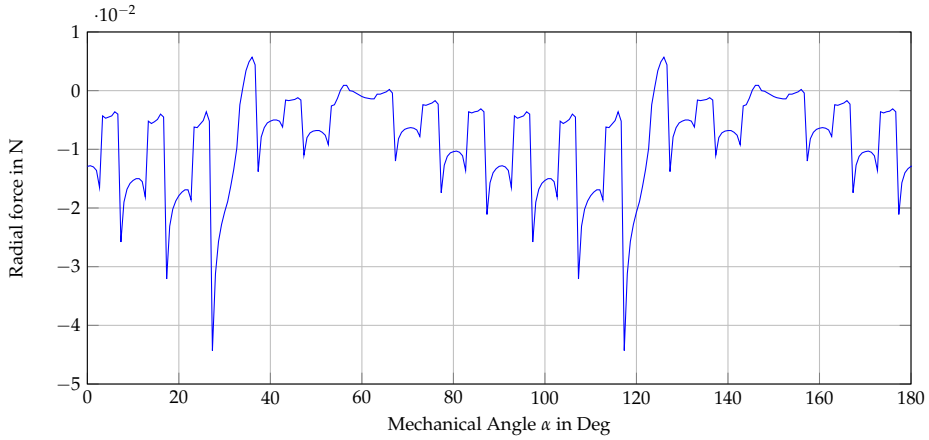

Figure 16. Radial force component at the stator teeth as a function of mechanical angle for one time step at a rated power of 49 kW and a rotational speed of 8540 rpm.

The forces acting in the air gap lead to structural vibrations of the stator. In combination with the eigenmodes and eigenfrequencies of the structure, which were obtained from a computational modal analysis (not shown here for brevity) according to the schematic shown in Figure 14, the equivalent radiated power of the electric motor can be calculated. Figure 17 shows this ERP for the selected operating point as a function of frequency. The frequency is given in multiples of the electrical frequency of approximately 285 Hz. It can be seen that the ERP has maxima around 5 kHz with peak levels of approximately 70 dB, as well as corresponding harmonics around 10 kHz and 15 kHz. Although overall the level appears quite low, it is possible that such high-frequency components could affect the total noise from the vehicle and, especially, psychoacoustic metrics such as tonality and sharpness.

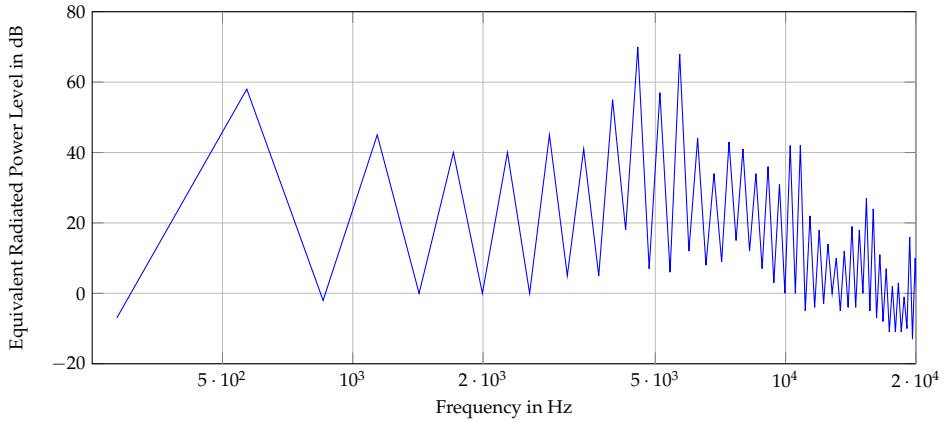

Figure 17. Equivalent radiated power (ERP) level of the example electric machine shown in Figure 14 at a rated power of 49 kW and a rotational speed of 8540 rpm.

It has to be noted that the ERP is a measure of the structure-borne sound power, and the part of the ERP that is radiated into the acoustic far field further depends on the radiation efficiency as well as on secondary effects such as possible shielding by the nacelle. In addition, the mounting of the motor and other connected components will affect the vibrational behavior and hence the eigenfrequencies. However, the ERP presented in Figure 17 is still a valuable indicator of frequency ranges where tonal noise from the electric machine may add to the total noise of the propulsion system.

6. Tip Rotor

6.1. Method

Based on the thrust requirements during the mission of the vehicle, a set of propellers for the tilt-rotor vehicle are designed. For this purpose, an inverse propeller design method is used. This method is based on classical blade-element-momentum theory (BEMT) [70–76] and delivers the blade geometry, which is automatically translated into a computer-aided design (CAD) geometry. For exploring the design space, several parameter variations with respect to diameter, rotational speed and blade twist are performed. The final design is a compromise between the cruise case, where a highly twisted blade shape is desired, and the hover case, where a very low twist is required (see Table 5 for the final operating conditions). The result depends on the ratio of the mission energy used during hover to the energy used for the cruise segment. The main design point was therefore biased towards the hover case. Additional constraints like tip Mach number and trailing edge thickness were taken into account.

Table 5. Tilt-rotor operating conditions.

	Cruise	Hover	Units
D	1.85	1.85	m
C_P	0.308	0.120	-
C_T	0.122	0.210	-
$\beta_{0.75}$	42.3	17.5	°
n	840	1828	1/min
η	85.2	–	%
T/P	–	29.8	N/kW
M_{tip}	0.300	0.521	-

It is not possible to cover the operating regime with a fixed pitch propeller having reasonable efficiency. Therefore, the design uses two blade angle settings, $\beta_{0.75} = 42°$ and 17.5°, for cruise and hover, respectively. In order to keep noise levels due to compressibility low, the design is performed for $M_{tip} = 0.30$ in cruise and $M_{tip} = 0.52$ in hover. A blade count of five is chosen to obtain reasonable chord lengths and low vibration levels in the transition phase. The geometry of the preliminary propeller design (see Figure 18) is used to generate a CAD model for subsequent analysis by Computational Fluid Dynamics (CFD) and a refinement of the blade angle settings for the full scale as well as for the model propeller.

For the planned wind tunnel measurements in the next phase of the project, a scaled model of the propeller is necessary. As is generally the case in the testing of scaled models, complete aerodynamic similarity is difficult to attain, and here, the goal is to match the advance ratio and to maintain the same tip Mach number and radial loading. Due to the scaling laws, the Reynolds number cannot be matched, though. It is reduced by the scale factor. While the airfoil sections in the full-scale propeller operate at up to $Re = 5 \times 10^5$, the Reynolds numbers on the 21.6 % scale model propeller drop to below $Re = 1 \times 10^5$. In the experiments, measures will be taken to ensure that the flow remains attached, which

can be done by the use of flow visualization techniques as well as by the application of tripping tape to ensure the boundary layer transition.

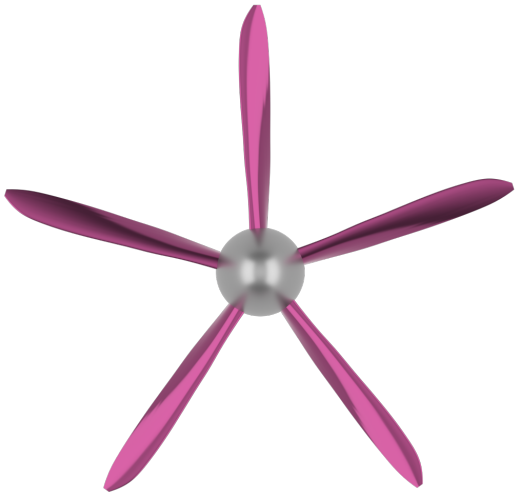

Figure 18. Tilt-rotor with blade angle set for hover.

An experimental evaluation of the scaled tilt-rotor aerodynamic performance and acoustic emissions will be performed in the Acoustic Wind tunnel Braunschweig (AWB) [77]. The AWB has a nozzle area of 0.8×1.2 m^2 and thus allows testing of rotors with diameters up to approximately 0.4 m, corresponding to a scaling factor, i.e., full-scale to model-scale diameter ratio, of 0.216, as mentioned above. For manufacturability reasons, the thickness of the blade's trailing edge is a constraint set to the rotor design. The model scale blade design needs to have a small trailing-edge-to-boundary-layer thickness ratio to mitigate bluntness noise generation due to the ejection of a von Kármán vortex sheet as the flow passes the blade's trailing edge. The model rotor design will have a freely adjustable blade pitch angle to allow for a variable and precise adjustment of the hover and cruise configuration-specific blade settings. It is planned to capture the acoustic emissions directivity of the tilt-rotor setup using a large array of free-field microphones.

6.2. Results

The propeller, as designed using the BEMT-based approach, is subsequently verified in RANS studies utilizing the DLR TAU-Code [61,62], which has been widely applied and validated for the design and analysis of various propeller and open rotor configurations (see, for example, [78,79]). These steady-state simulations in the rotating reference frame of the propeller, a sample result of which is shown in Figure 19, are done with fully turbulent flow prescribed using the one-equation Spalart–Allmaras (SA) turbulence model. The results confirm the quality of the propeller design, showing, for example, that for the cruise condition the target thrust can be obtained at an efficiency of 83.1%, a value very close to the BEMT model prediction specified in Table 5. The slight offset is fully expected and caused by 3D effects that are included in the RANS simulations but not captured in their entirety in the BEMT approach.

As the aim of the project is to measure the noise signature of the propeller as a tip-mounted propulsor in a wind tunnel for further exploitation in the auralization of typical UAM noise emissions, the RANS studies also focused on analyzing and understanding scale/Reynolds number effects on the propeller performance and noise signature.

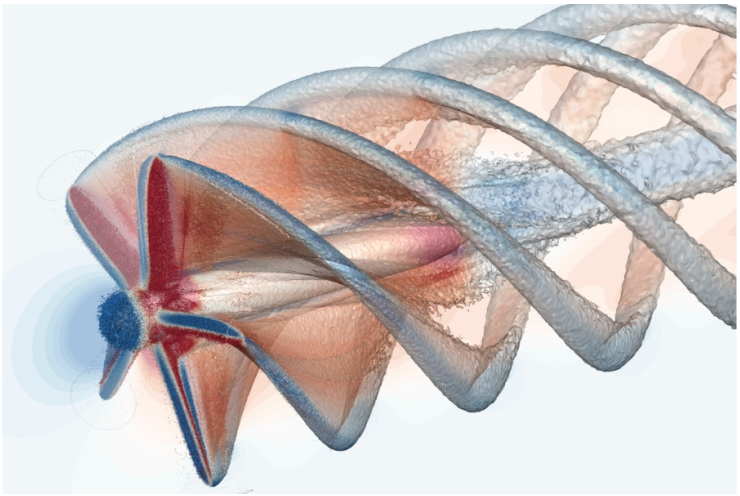

Figure 19. RANS simulation result of the isolated tilt-rotor propeller at cruise conditions

For both the cruise and hover operating points, a 1:5-scaled version of the propeller is simulated at typical sea-level conditions using the same TAU-Code RANS approach applied in the full-scale propeller analysis while keeping the Mach number and advance ratio the same. For the example of the cruise condition, the scale effects manifest in the blade suction side flow topology in terms of a slightly more pronounced flow separation at the blade hub for the sub-scale propeller, as can be seen in Figure 20.

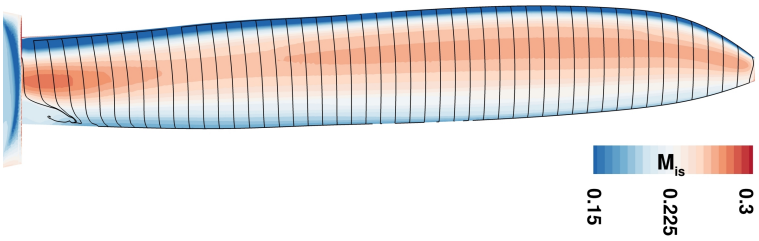

(**a**) Full-scale blade suction side.

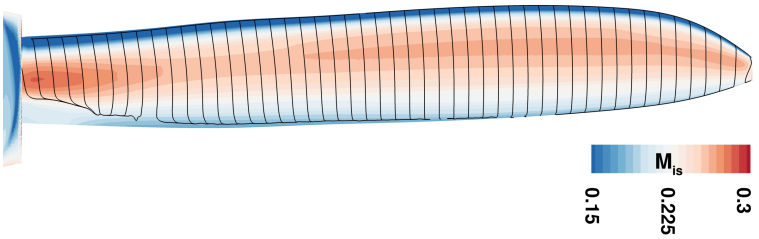

(**b**) Model-scale blade suction side.

Figure 20. Scale effects on blade aerodynamics at identical blade pitch and operating point.

The viscous decambering effects of the reduced Reynolds number, which occur for the model-scale versus the full-scale geometry, have a clear impact on the mean propeller performance metrics, as plotted in Figure 21. In order to achieve the target thrust coefficient value, the sub-scale propeller must operate at an increased blade pitch. For the example of the cruise operating point shown here, only a relatively small pitch increase of 0.5° is required.

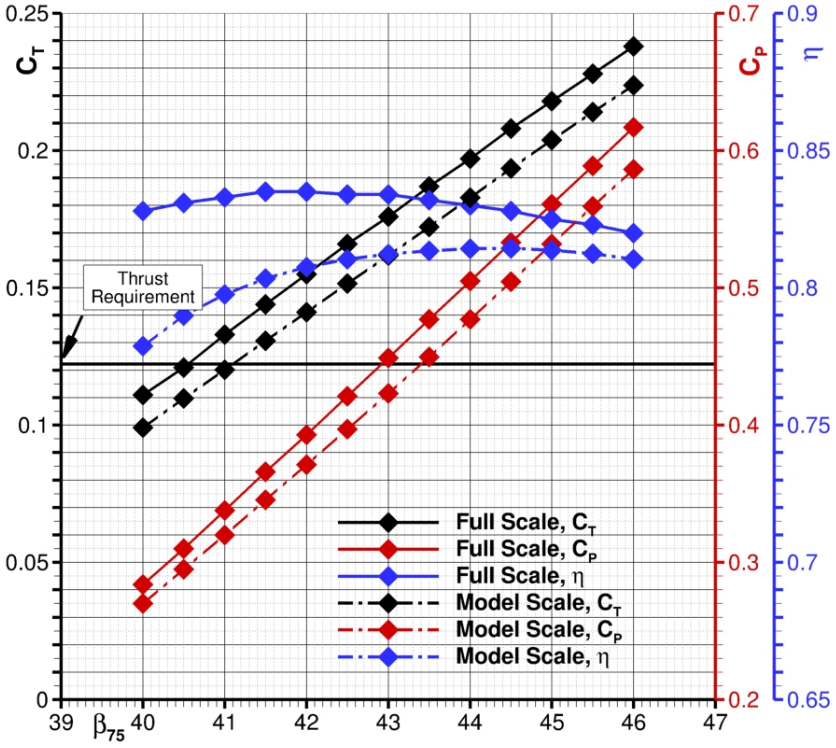

Figure 21. Reynolds number effects on the cruise performance of the propeller.

Figure 22 presents a comparison of the blade radial thrust distribution. The reference full-scale result at the blade pitch angle for which the target thrust coefficient is achieved is compared to model-scale blade results at the two blade pitches of $\beta_{75} = 40.5°$ and $\beta_{75} = 41°$. The latter two results show that the increased extent of the hub trailing edge flow separation at model scale, as noted above, leads to a thrust loss for inboard regions of the model-scale propeller. This must be compensated for through an increased thrust production near the tip by operating at a slightly larger blade pitch angle of around $\beta_{75} = 41°$ for the sub-scale propeller versus $\beta_{75} = 40.5°$ for the full-scale propeller to achieve the target thrust coefficient.

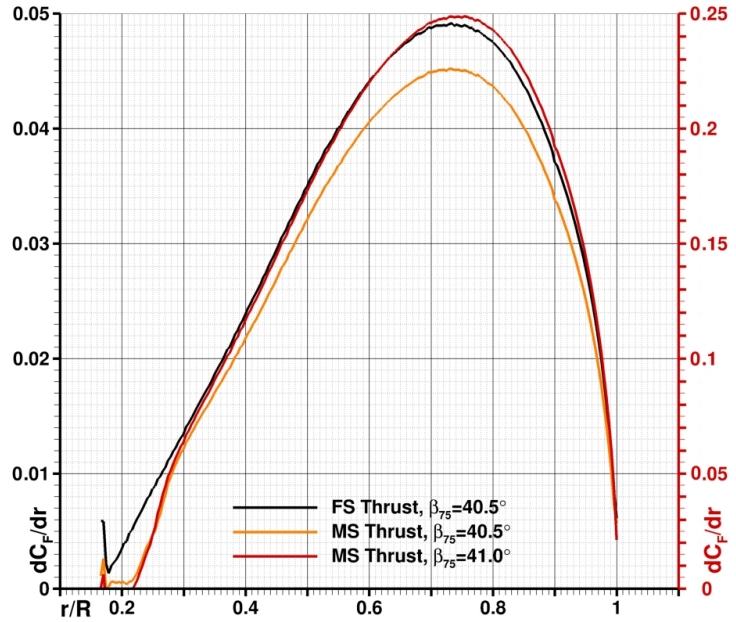

Figure 22. Reynolds number effects on the radial thrust distribution of the blade at cruise conditions.

A comparison of the total radial loading distribution, not shown here, is very similar to the thrust-component-only distribution in Figure 22, and is one of the key characteristics defining propeller noise emissions. With the slight outboard shift of the peak loading for the model-scale versus the full-scale propeller at an identical thrust coefficient, achieving acoustic similarity between the two may necessitate operating the sub-scale propeller at a slightly lower blade pitch and thrust coefficient.

Further RANS studies will be performed in this project as needed to guide and support both the design of the wind tunnel models and their operation in the acoustic tests to help ensure that the quality of the obtained measurements meets the project requirements.

7. Ducted Fan

7.1. Method

The acoustic spectrum of a fan is generated by several tonal and broadband noise sources. For low-speed fan stages, rotor–stator interaction noise, particularly its tonal component, typically represents the primary source of noise. Commonly, the noise generation spectrum is predominantly affected by the tone at the blade passing frequency (BPF) and its harmonics.

For the propulsion system of the tilt-duct vehicle, two fan stages with fewer stator than rotor blades (low-count OGV (outer guide vane) fans) are designed, whereby two acoustic effects are applied to reduce the tonal noise levels at source. It is particularly relevant to demonstrate tonal noise reduction mechanisms on low-count OGV fans, as a disadvantage regarding tonal noise for these fans exists. The reason is that the usually dominant blade passing frequency tone is generally no longer cut off, since fewer stator than rotor blades are used. However, at low rotor tip Mach numbers certain rotor blade count combinations exist, for which a cut-off can still be achieved even though the stator vane count is lower than the rotor blade count. This effect is called inverse cut-off [80,81] and can exclusively be applied to low-speed fans since the rotor tip Mach number needs to be lower than the critical Mach number, as derived in [82]. Since this condition is achieved for the targeted low-count OGV fans, the inverse cut-off effect is the first applied tonal noise reduction mechanism.

For the second low-count OGV fan stage, however, the blade and vane numbers are chosen such that the inverse cut-off condition is not reached. Therefore, in order to reduce the noise excitation at the BPF tone, an additional effect is applied. This effect relies on a carefully chosen rotor–stator blade count to mitigate tonal noise excitation, even when the BPF is cut-on. The underlying physical mechanism of this effect is associated with the propagation direction of the excited acoustic waves relative to the dipole radiation axis. When acoustic energy propagates perpendicularly to the dipole radiation axis, the excitation of acoustic energy is reduced [83]. Since the propagation direction is controlled by the excited acoustic interaction modes, which in turn depend on the blade count (see [84]), this effect can be achieved through a well-devised selection of the rotor–stator blade counts. Duncan and Dawson [83] named this mechanism the "Venetian blind" effect, and Schade et al. [85] demonstrated that the effect can be applied to a low-count OGV fan on the condition that the subsequent design rule is fulfilled. The design rule expresses the expected tonal noise reduction in dB as a function of Δ,

$$20 \log_{10}(\sin(|\Delta|)) \text{ dB}, \tag{2}$$

where Δ is the difference between the stator leading edge angle and the propagation direction of the dominant acoustic interaction mode [85]. As Equation (2) indicates, the tonal excitation of the rotor–stator interaction noise source can be significantly reduced if the propagation direction of the dominantly excited mode is aligned with the stator leading

edge angle ($\sin(|\Delta|) \rightarrow 0$). This is analytically and numerically investigated and experimentally confirmed in [85].

In the presented fan pre-design process, the stator leading edge angle is fixed, as it is defined by the aerodynamic flow conditions within the duct segments of the fan stage. Therefore, the propagation direction of the dominant mode is the degree of freedom with which the acoustic effect can be controlled. As described above, since this propagation direction is defined by the mode order and the mode order in turn depends on the rotor and stator blade numbers, the noise reduction is achieved with a smart selection of rotor and stator blade numbers. To evaluate which blade count combinations are suitable, blade count variations are performed using the analytical in-house noise prediction tool PropNoise (Propulsion Noise) [43]. The results of these blade count variations are presented in [85].

The two low-count OGV fan stages are designed and manufactured for experimental testing in the CRAFT (Co-/Contra Rotating Acoustic Fan Test) facility [86]. In this facility, ducted fan stages with representative conditions (e.g., rotor tip Mach number and fan pressure ratio) for UAM engines can be examined.

The tilt-duct vehicle, described in Section 3, performs the take-off and landing flight phases vertically. Therefore, the fan stages are operated within a wide range of operating conditions as the aerodynamic flow might strongly deviate between vertical and horizontal flight. In order to handle these different operating regimes, a conceptual design of a variable-area nozzle (VAN) is performed according to the method described in [87]. Table 6 shows the fan operating conditions at cruise and take-off with and without VAN for the baseline fan geometry, and additional details regarding VAN design can be obtained from [46].

Table 6. Fan operating conditions.

	Cruise	**Take-Off**	**Take-Off VAN**
nozzle area	+0 %	+0 %	+30 %
n/rpm	3375	8540	7995
$\dot{m}$/(kg/s)	5.25	10.7	12.3
M_{tip}	0.26	0.64	0.61
PR	1.021	1.177	1.133
η_{is}/%	90.0	88.0	91.5
thrust/kN	2.1	30	30

7.2. Results

The tilt-duct vehicle is equipped with 26 low-speed fan stages, of which 10 fans are located on the canard wing and 16 on the main wing. Each fan has a diameter of 0.46 m and three fan designs are available, a baseline fan (see Figure 23a), a low-tonal-noise fan (Figure 23c) and a low-broadband-noise fan (Figure 23b), of which the latter two are the designed low-count OGV fan stages, as outlined in Section 7.1. The selected blade count combinations of all three fan designs are listed in Table 7.

(**a**) baseline (**b**) low-broadband (**c**) low-tone

Figure 23. Geometry of the different fan designs.

Table 7. Fan rotor and stator blade numbers.

	Baseline	Low-Tone	Low-Broadband
rotor	18	31	31
stator	21	21	10

Figure 24 compares the tonal noise directivities between the three fan designs at design operating conditions (n = 4500 rpm, $\dot{m} = 7.0\,\mathrm{kg/s}$, $M_{\mathrm{tip}} = 0.31$). The sound pressure levels (L_p) are plotted on a hemisphere with a radius of 100 m. The energetic sum of the noise contributions at the dominant tonal frequencies is shown. At design operating conditions, the first BPF is 1350 Hz for the baseline fan. For the low-broadband and low-tone fans, the first BPF increases to 2325 Hz due to the higher rotor blade count (see Table 7). Note that the tone at the first BPF (2325 Hz) is inverse cut-off for the low-tone fan, as outlined in Section 7.1. The fan stage is located at $x, y, z = 0\,\mathrm{m}$. The axial angle is ϕ, where $\phi = 180$ indicates the upstream direction and $\phi = 0$ the downstream direction, and the lateral angle is θ.

For the baseline fan stage (see Figure 24a), tonal noise is the dominant source for all radiation angles. The dominant tonal noise radiation direction and also the dominant overall noise radiation direction are downstream at $\phi = 50$.

For the low-broadband-noise fan stage (see Figure 24b), an opposite tonal characteristic is observed compared to the baseline fan. The dominant tonal noise radiation direction is upstream, with the maximum radiation angles at $\phi = 135$ and $\phi = 165$. For the aural experience, this means that the baseline fan radiates tonal noise throughout the entire flyover. The highest tonal sound pressure levels occur when the vehicle has already passed the observer. By contrast, in the case of the low-broadband fan, the fan tones can be detected before the vehicle has passed but are masked by broadband noise after the vehicle has passed. The reason for the downstream tonal noise reduction is that the blade numbers are chosen such that the propagation angle of the dominantly excited tonal mode is almost parallel to the stator leading edge angle, as outlined in Section 7.1 and in [85].

Regarding the low-tonal-noise fan design (see Figure 24c), two acoustic effects are applied in order to achieve a significant tonal noise reduction: Firstly, similar to the low-broadband-noise fan stage, the blade numbers are chosen such that the propagation angle of the dominantly excited tonal mode is almost parallel to the stator leading edge angle. However, the tonal noise reduction achieved is now directed upstream. This means that for the low-tonal-noise fan stage, this effect is used to reduce the upstream radiation of tonal noise, while for the low-broadband-noise fan stage the same effect is used to reduce tonal noise downstream. Therefore, the effect of aligning the propagation of the dominant mode with the stator leading edge can be used to control the tonal noise radiation characteristic [85].

Secondly, as the rotor tip Mach number is low enough, the blade numbers are chosen such that the first BPF tone is inverse cut-off [82,85], resulting in an additional tonal noise reduction. Due to these acoustic effects, the tonal sound pressure levels are similar to or even lower than the broadband levels over all radiation angles. For the aural experience, this means that tonal noise is almost fully masked by broadband noise, resulting in a rather hissing-sounding aural impression.

The noise directivities in Figure 24 are shown for a single fan. For the tilt-duct vehicle, 26 of these fans are combined to form the distributed propulsion system. Due to the large number of fan stages, it can be expected that the noise directivities of the distributed fan system will differ from that of the individual fan. For example, interferences are expected that result from interactions between the 26 sound fields, so that the noise directivities of the overall system may contain complex interference patterns. For the aural experience,

this means that the noise signature may vary considerably depending on the observer's position and that spectral as well as temporal fluctuations may exist. The impact of the three fan designs on the psychoacoustic characteristics of the distributed propulsion system of the tilt-duct vehicle is investigated in [46].

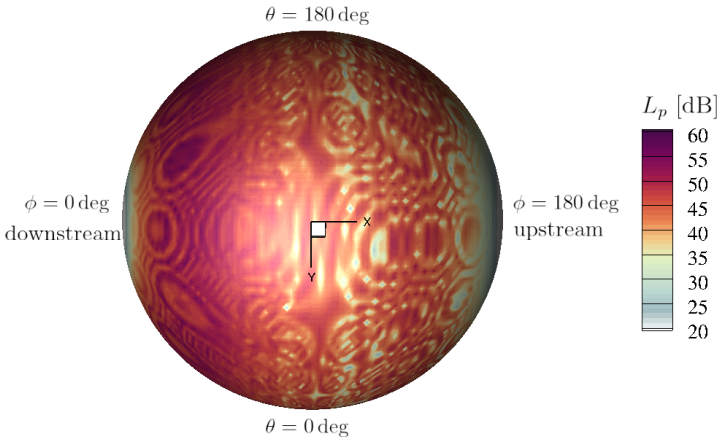

(**a**) baseline

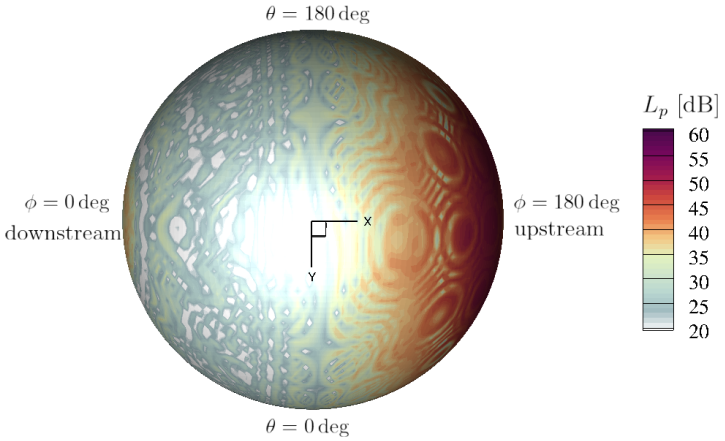

(**b**) low-broadband

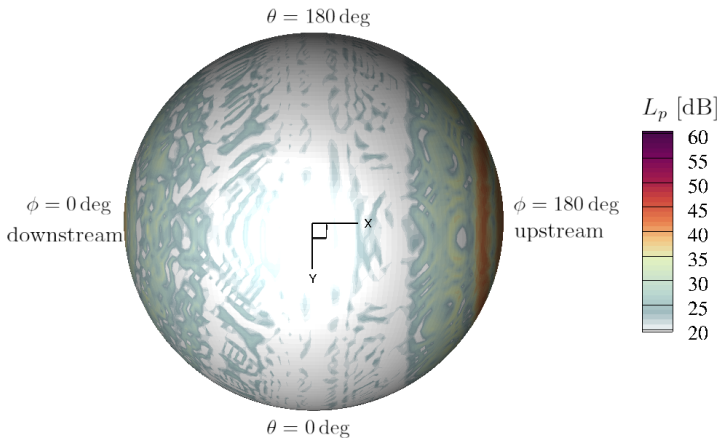

(**c**) low-tone

Figure 24. Tonal noise directivities plotted on a hemisphere of radius 100 m for the different fan designs.

Table 8 compares the aerodynamic performance of the three fan designs in terms of their efficiency η_{is} and their pressure ratio (PR) at design as well as cruise operating conditions and verifies that the different fan stages provide similar aerodynamic characteristics.

Table 8. Aerodynamic performance of the three fan stages.

		Baseline	Low-Tone	Low-Broadband
Design	η_{is}	90.4	90.2	90.0
	PR	1.0382	1.0396	1.0382
Cruise	η_{is}	90.0	89.8	90.0
	PR	1.0210	1.0218	1.0217

As an intermediate conclusion, the fan stages are aerodynamically similar but show very different noise radiation characteristics. Thus, the fan stages are well-suited for acoustic as well as psychoacoustic assessments regarding the impact of the fan design on the noise radiation of a distributed propulsion system. Results from psychoacoustic studies focusing on the effect of rotational speed fluctuations are given in [47].

8. Summary and Outlook

The noise generated by the variety of existing concepts for novel eVTOL vehicles as well as its subsequent psychoacoustic effect on humans will be a major factor influencing public acceptance and corresponding economical success. As such, vehicles currently are, for the most part, still in development. The aim of the present study is to provide a basis for the future analysis and evaluation of different vehicle designs in noise tests with human subjects. Therefore, the main focus is on distributed electric propulsion systems using either open rotors or ducted fans that are driven by electric motors, and the subsequent interaction of sound originating from these different sources.

In order to enable such analyses, two different UAM vehicle designs were developed as part of an ongoing research study. Both have identical missions, loads and estimated entry into service but different electric propulsion systems. One vehicle is powered by a set of tiltable open rotors and one by tiltable ducted fans. For both concepts, three different powertrain topologies were configured: (1) a fully battery-electric propulsion system, (2) a fully fuel-cell powered propulsion system and (3) a hybrid system with varying degrees of hybridization. For the tilt-rotor vehicle, a propeller was designed that is able to deliver the required thrust in all phases of the mission. The aerodynamic performance of this propeller was evaluated in detailed RANS simulations, while its corresponding noise generation will be analyzed in wind tunnel experiments in the next phase of the project. For the planned acoustic measurements on ducted fan stages that represent the tilt-duct propulsion system, two low-count OGV fans were designed, one that is characterized by a notable reduction in tonal noise compared to the baseline fan and another that leads to reduced broadband noise levels. It should again be emphasized here that the current report aims to give an overview of the necessary considerations and methods involved in the design of the two concept vehicles and their propulsion systems, with the aim of providing a basis for future acoustic studies. More details on each of the design steps are provided in the additional literature mentioned in the corresponding sections.

As a prerequisite for the planned vehicle flyover auralizations, a set of detailed experiments will be performed on the different propulsion systems in the next step of the project. This includes acoustic measurements on a model-scale tip propeller configuration in an aeroacoustic wind tunnel, acoustic measurements on the two low-count OGV fan stages in a dedicated fan test rig and measurements on an electric motor as a representation of the electric powertrain.

Author Contributions: Conceptualization: S.S. and T.F.G.; methodology: S.S., J.L., P.R., M.H., A.S., P.S. and T.F.G.; formal analysis and investigation: S.S., J.L., P.R., M.H., A.S. and P.S.; writing—original draft preparation: S.S., J.L., P.R., M.H., A.S. and T.F.G.; writing—review and editing: S.S., J.L., P.R.,

M.H., A.S. and T.F.G.; supervision: S.S., K.-S.R., S.d.G. and T.F.G. All authors have read and agreed to the published version of the manuscript.

Funding: This publication is part of the project *VIRLWINT* (https://www.dlr.de/en/at/research-transfer/projects/virlwint) (virtual acoustic twin of distributed propulsion systems) funded by the German Aerospace Center.

Data Availability Statement: The data are available from the authors upon request.

Acknowledgments: The authors thank Martin Staggat (formerly DLR, Institute of Electrified Aero Engines), Lukas Klähn (DLR, Institute of Propulsion Technology) and Vivek Gupta (DLR, Institute of Electrified Aero Engines). This article is an extended version of our paper published in Deutscher Luft- und Raumfahrtkongress (DLRK) 2024 [88].

Conflicts of Interest: The authors declare no conflicts of interest.

Symbols and Abbreviations

The following symbols and abbreviations are used in this manuscript:

L_p	sound pressure level, dB
H_p	degree of hybridization
D	diameter, m
C_P	power coefficient
C_T	thrust coefficient
C_F	force coefficient
β_{75}	blade pitch angle, deg
n	rotational speed, rpm
η	efficiency
T	thrust, N
P	power, W
r, R	radial position, propeller radius, m
M_{is}	isentropic Mach number
M_{tip}	rotor tip Mach number
$\dot{m}$	mass flow, kg/s
ϕ	axial directivity angle, deg
θ	lateral directivity angle, deg
Δ	difference between stator leading edge and modal propagation angle
ANOPP	Aircraft Noise Prediction Program
AWB	Acoustic Wind tunnel Braunschweig
BEMT	blade-element-momentum theory
BPF	blade passing frequency
CAD	computer-aided design
CFD	Computational Fluid Dynamics
CORAL	aircraft engine noise auralization
CRAFT	Co-/Contra Rotating Acoustic Fan Test rig
DC	direct current
DEP	distributed electric propulsion
DLR	German Aerospace Center
EDT	rlectric drivetrain
EIS	rntry into service
EPNL	rffective perceived noise level
ERP	rquivalent radiated power
eVTOL	electric Vertical Take-Off and Landing
FCS	fuel cell system
FEM	Finite Element Method

FS	full scale
INSTANT	Integrated Noise Simulation and Assessment module
MS	model scale
MTOM	Maximum Take-Off Mass
NASA	National Aeronautics and Space Administration
OGV	outer guide vane
PANAM	Parametric Aircraft Noise Analysis Module
PMSM	Permanent Magnet Synchronous Machine
PR	pressure ratio
PropNoise	PropulsionNoise
RANS	Reynolds-Averaged Navier Stokes
SA	Spalart–Allmaras
TLARs	Top-Level Aircraft Requirements
TMS	thermal management system
UAM	urban air mobility
VAN	variable-area nozzle
VIOLIN	virtual acoustic flyover simulation
VTOL	Vertical Take-Off and Landing

References

1. Johnson, W.; Silva, C.; Solis, E. Concept Vehicles for VTOL Air Taxi Operations. In Proceedings of the AHS Technical Conference on Aeromechanics Design for Transformative Vertical Flight, San Francisco, CA, USA, 16–19 January 2018; Technical Report ARC-E-DAA-TN50731. Available online: https://ntrs.nasa.gov/citations/20180003381 (accessed on 17 March 2026).
2. Whiteside, S.; Pollard, B.; Antcliff, K.; Zawodny, N.; Fei, X. *Design of a Tiltwing Concept Vehicle for Urban Air Mobility*; Technical Report NASA/TM–20210017971; NASA; Langley Research Center: Hampton, VA, USA, 2021. Available online: https://ntrs.nasa.gov/citations/20210017971 (accessed on 17 March 2026).
3. Bacchini, A.; Cestino, E. Electric VTOL configurations comparison. *Aerospace* **2019**, *6*, 26. [CrossRef]
4. Afonso, F.; Ferreira, A.; Ribeiro, I.; Lau, F.; Suleman, A. On the design of environmentally sustainable aircraft for urban air mobility. *Transp. Res. Part D Transp. Environ.* **2021**, *91*, 102688. [CrossRef]
5. Mittal, P.; Alam, M.I. Design and Development of Personal Air Vehicles: A Review. In *Recent Trends in Mechanical Engineering: Select Proceedings of PRIME 2021*; Springer: Singapore, 2023; pp. 791–798. [CrossRef]
6. Nathen, P.; Strohmayer, A.; Miller, R.; Grimshaw, S.; Taylor, J. *Architectural Performance Assessment of an Electric Vertical Take-Off and Landing (e-VTOL) Aircraft Based on a Ducted Vectored Thrust Concept*; Technical Report; Lilium GmbH: Gauting, Germany, 2021.
7. Pak, H.; Asmer, L.; Kokus, P.; Schuchardt, B.I.; End, A.; Meller, F.; Schweiger, K.; Torens, C.; Barzantny, C.; Becker, D.; et al. Can Urban Air Mobility become reality? Opportunities and challenges of UAM as innovative mode of transport and DLR contribution to ongoing research. *CEAS Aeronaut. J.* **2025**, *16*, 665–695. [CrossRef]
8. Kim, H.D.; Perry, A.T.; Ansell, P.J. A Review of Distributed Electric Propulsion Concepts for Air Vehicle Technology. In Proceedings of the 2018 AIAA/IEEE Electric Aircraft Technologies Symposium, Cincinnati, OH, USA, 9 July–11 July 2018. [CrossRef]
9. Green, M.; Schiltgen, B.; Gibson, A. Analysis of a Distributed Hybrid Propulsion System with Conventional Electric Machines. In Proceedings of the 48th AIAA/ASME/SAE/ASEE Joint Propulsion Conference & Exhibit, Atlanta, GA, USA, 30 July–1 August 2012. [CrossRef]
10. Brelje, B.J.; Martins, J.R. Electric, hybrid, and turboelectric fixed-wing aircraft: A review of concepts, models, and design approaches. *Prog. Aerosp. Sci.* **2019**, *104*, 1–19. [CrossRef]
11. Silva, C.; Johnson, W.R.; Solis, E.; Patterson, M.D.; Antcliff, K.R. VTOL Urban Air Mobility Concept Vehicles for Technology Development. In Proceedings of the 2018 Aviation Technology, Integration, and Operations Conference, Atlanta, GA, USA, 25–29 June 2018. [CrossRef]
12. Silva, C.; Johnson, W. Practical Conceptual Design of Quieter Urban VTOL Aircraft. In Proceedings of the Vertical Flight Society's 77th Annual Forum & Technology Display, Virtual Event, 10–14 May 2021. Available online: https://ntrs.nasa.gov/citations/20210014173 (accessed on 17 March 2026).
13. Patterson, M.D.; Antcliff, K.R.; Kohlman, L.W. A Proposed Approach to Studying Urban Air Mobility Missions Including an Initial Exploration of Mission Requirements. In Proceedings of the AHS International 74th Annual Forum & Technology Display, Phoenix, AZ, USA, 14–17 May 2018; Technical Report NF1676L-28586. Available online: https://ntrs.nasa.gov/citations/20190000991 (accessed on 17 March 2026).

14. Antcliff, K.; Whiteside, S.; Kohlman, L.W.; Silva, C. Baseline Assumptions and Future Research Areas for Urban Air Mobility Vehicles. In Proceedings of the AIAA Scitech 2019 Forum, San Diego, CA, USA, 7–11 January 2019. [CrossRef]
15. Gutin, L. On the sound field of a rotating propeller. *Phys. Z. Sowjetunion (Phys. Mag. Sov. Union)* **1948**, *9*, 57–71.
16. Farassat, F.; Succi, G.P. A review of propeller discrete frequency noise prediction technology with emphasis on two current methods for time domain calculations. *J. Sound Vib.* **1980**, *71*, 399–419. [CrossRef]
17. Hanson, D.B. Influence of propeller design parameters on far-field harmonic noise in forward flight. *AIAA J.* **1980**, *18*, 1313–1319. [CrossRef]
18. Metzger, F.B. *A Review of Propeller Noise Prediction Methodology: 1919–1994*; Technical Report Contractor Report 198156; NASA; Langley Research Center: Hampton, VA, USA, 1995. Available online: https://ntrs.nasa.gov/citations/19960008819 (accessed on 17 March 2026).
19. Rumsey, C.L.; Biedron, R.T.; Farassat, F.; Spence, P.L. Ducted-fan engine acoustic predictions using a Navier–Stokes code. *J. Sound Vib.* **1998**, *213*, 643–664. [CrossRef]
20. Bennett, G.J.; Fitzpatrick, J.A. Noise-source identification for ducted fan systems. *AIAA J.* **2008**, *46*, 1663–1674. [CrossRef]
21. De Laborderie, J.; Moreau, S. Prediction of tonal ducted fan noise. *J. Sound Vib.* **2016**, *372*, 105–132. [CrossRef]
22. Moreau, A.; Guérin, S. The impact of low-speed fan design on noise: An exploratory study. *J. Turbomach.* **2016**, *138*, 081006. [CrossRef]
23. Borer, N.K.; Patterson, M.D.; Viken, J.K.; Moore, M.D.; Bevirt, J.; Stoll, A.M.; Gibson, A.R. Design and Performance of the NASA SCEPTOR Distributed Electric Propulsion Flight Demonstrator. In Proceedings of the 16th AIAA Aviation Technology, Integration, and Operations Conference, Washington, DC, USA, 13–17 June 2016. [CrossRef]
24. Boucher, M.; Rafaelof, M.; Begault, D.; Christian, A.; Krishnamurthy, S.; Rizzi, S. A Psychoacoustic Test for Urban Air Mobility Vehicle Sound Quality. *SAE Int. J. Adv. Curr. Prac. Mobil.* **2024**, *6*, 972–985. [CrossRef]
25. Bernardini, G.; Centracchio, F.; Gennaretti, M.; Iemma, U.; Pasquali, C.; Poggi, C.; Rossetti, M.; Serafini, J. Numerical Characterisation of the Aeroacoustic Signature of Propeller Arrays for Distributed Electric Propulsion. *Appl. Sci.* **2020**, *10*, 2643. [CrossRef]
26. Guérin, S.; Tormen, D. A contribution to the investigation of acoustic interferences in aircraft distributed propulsion. *CEAS Aeronaut. J.* **2023**, *14*, 965–982. [CrossRef]
27. Bolam, R.C.; Vagapov, Y.; Anuchin, A. A review of electrical motor topologies for aircraft propulsion. In *Proceedings of the 2020 55th International Universities Power Engineering Conference (UPEC)*; IEEE: Piscataway, NJ, USA, 2020; pp. 1–6. [CrossRef]
28. Rizzi, S.A.; Huff, D.L.; Boyd, D.D.; Bent, P.; Henderson, B.S.; Pascioni, K.A.; Sargent, D.C.; Josephson, D.L.; Marsan, M.; He, H.; et al. *Urban Air Mobility Noise: Current Practice, Gaps, and Recommendations*; NASA/TP-2020-5007433; NASA; Langley Research Center: Hampton, VA, USA, 2020. Available online: https://ntrs.nasa.gov/citations/20205007433 (accessed on 17 March 2026).
29. Pascioni, K.A.; Watts, M.E.; Houston, M.; Lind, A.; Stephenson, J.H.; Bain, J. Acoustic flight test of the joby aviation advanced air mobility prototype vehicle. In Proceedings of the 28th AIAA/CEAS Aeroacoustics 2022 Conference, Southampton, UK, 14–17 June 2022; AIAA Paper 2022-3036.
30. Thai, A.; Bain, J.; Mikić, G.V.; Stoll, A. Flyover Noise Computations of the Joby Aviation Aircraft. In Proceedings of the Vertical Flight Society 79th Annual Forum & Technology Display, West Palm Beach, FL, USA, 16–18 May 2023.
31. Thai, A.; Bain, J. Modeling Approach and Departure Noise of the Joby Aviation Aircraft. In Proceedings of the Vertical Flight Society 80th Annual Forum, Montréal, QC, Canada, 7–9 May 2024.
32. Schatzman, N.L.; Weist, L.; Bain, J.J.; Thai, A.D. Acoustic Testing of the Joby Aviation Propeller in the National Full-Scale Aerodynamics Complex 40-by 80-Foot Wind Tunnel. In Proceedings of the AIAA SCITECH 2025 Forum, Orlando, FL, USA, 6–10 January 2025; AIAA Paper 2025-0844.
33. Iemma, U.; Diez, M. Optimal conceptual design of aircraft including community noise prediction. In Proceedings of the 12th AIAA/CEAS Aeroacoustics Conference (27th AIAA Aeroacoustics Conference), Cambridge, MA, USA, 8–10 May 2006; AIAA Paper 2006-2621.
34. Rizzi, S.A.; Aumann, A.R.; Lopes, L.V.; Burley, C.L. Auralization of hybrid wing–body aircraft flyover noise from system noise predictions. *J. Aircr.* **2014**, *51*, 1914–1926. [CrossRef]
35. Rizzi, S.A. Toward reduced aircraft community noise impact via a perception-influenced design approach. In Proceedings of the Inter-Noise and Noise-Con Congress and Conference Proceedings, Hamburg, Germany, 21–24 August 2016. Available online: https://ntrs.nasa.gov/citations/20160011152 (accessed on 17 March 2026).
36. Rizzi, S.A.; Palumbo, D.L.; Rathsam, J.; Christian, A.W.; Rafaelof, M. Annoyance to noise produced by a distributed electric propulsion high-lift system. In Proceedings of the 23rd AIAA/CEAS Aeroacoustics Conference, Denver, CO, USA, 5–9 June 2017; AIAA Paper 2017-4050. [CrossRef]
37. Brentner, K.S.; Lopes, L.V.; Chen, H.N.; Horn, J.F. Near real-time simulation of rotorcraft acoustics and flight dynamics. *J. Aircr.* **2005**, *42*, 347–355. [CrossRef]

38. Sahai, A.K.; Snellen, M.; Simons, D.G.; Stumpf, E. Aircraft design optimization for lowering community noise exposure based on annoyance metrics. *J. Aircr.* **2017**, *54*, 2257–2269. [CrossRef]
39. Sahai, A.K.; Simons, D.; Stumpf, E. Consideration of Aircraft Noise Annoyance During Conceptual Aircraft Design. Ph.D. Thesis, Lehrstuhl und Institut für Luft-und Raumfahrtsysteme (ILR), Aachen, Germany, 2016. Available online: https://publications.rwth-aachen.de/record/668901?ln=de (accessed on 17 March 2026).
40. Wunderli, J.M.; Zellmann, C.; Köpfli, M.; Habermacher, M. Sonair—A GIS-integrated spectral aircraft noise simulation tool for single flight prediction and noise mapping. *Acta Acust. United Acust.* **2018**, *104*, 440–451. [CrossRef]
41. Wunderli, J.M.; Meister, J.; Boolakee, O.; Heutschi, K. A method to measure and model acoustic emissions of multicopters. *Int. J. Environ. Res. Public Health* **2022**, *20*, 96. [CrossRef]
42. Bertsch, L. Noise Prediction Within Conceptual Aircraft Design. Ph.D. Thesis, Technische Universität Braunschweig, Braunschweig, Germany, 2013.
43. Moreau, A. A Unified Analytical Approach for the Acoustic Conceptual Design of Fans of Modern Aero-Engines. Ph.D. Thesis, Technische Universität Berlin, Berlin, Germany, 2017. Available online: https://depositonce.tu-berlin.de/items/41b906de-82f7-4a42-9bef-0944afb6acd8 (accessed on 17 March 2026).
44. Pieren, R.; Le Griffon, I.; Bertsch, L.; Heusser, A.; Centracchio, F.; Weintraub, D.; Lavandier, C.; Schäffer, B. Perception-based noise assessment of a future blended wing body aircraft concept using synthesized flyovers in an acoustic VR environment—The ARTEM study. *Aerosp. Sci. Technol.* **2024**, *144*, 108767. [CrossRef]
45. Moreau, A.; Prescher, A.; Schade, S.; Dang, M.; Jaron, R.; Guérin, S. A framework to simulate and to auralize the sound emitted by aircraft engines. In Proceedings of the InterNoise Conference, Chiba, Japan, 20–23 August 2023; Conference Proceedings. [CrossRef]
46. Schade, S.; Merino-Martinez, R.; Moreau, A.; Bartels, S.; Jaron, R. Psychoacoustic evaluation of different fan designs for an urban air mobility vehicle with distributed propulsion system. *J. Acoust. Soc. Am.* **2025**, *157*, 2150–2167. [CrossRef]
47. Schade, S.; Merino-Martinez, R.; Ratei, P.; Bartels, S.; Jaron, R.; Moreau, A. Initial Study on the Impact of Speed Fluctuations on the Psychoacoustic Characteristics of a Distributed Propulsion System with Ducted Fans. In Proceedings of the 30th AIAA/CEAS Aeroacoustics Conference, Rome, Italy, 4–7 June 2024; AIAA Paper 2024-3273. [CrossRef]
48. Filippone, A. Aircraft noise prediction. *Prog. Aerosp. Sci.* **2014**, *68*, 27–63. [CrossRef]
49. Meister, J.; Schalcher, S.; Wunderli, J.M.; Jäger, D.; Zellmann, C.; Schäffer, B. Comparison of the aircraft noise calculation programs sonAIR, FLULA2 and AEDT with noise measurements of single flights. *Aerospace* **2021**, *8*, 388. [CrossRef]
50. Pieren, R.; Bertsch, L.; Lauper, D.; Schäffer, B. Improving future low-noise aircraft technologies using experimental perception-based evaluation of synthetic flyovers. *Sci. Total Environ.* **2019**, *692*, 68–81. [CrossRef] [PubMed]
51. Rizzi, S.; Christian, A. A Psychoacoustic Evaluation of Noise Signatures from Advanced Civil Transport Aircraft. In Proceedings of the 22nd AIAA/CEAS Aeroacoustics Conference, Lyon, France, 30 May–1 June 2016. [CrossRef]
52. EASA. Study on the Societal Acceptance of Urban Air Mobility in Europe, 2021. Available online: https://www.easa.europa.eu/sites/default/files/dfu/uam-full-report.pdf (accessed on 17 March 2026).
53. Vorländer, M. *Auralization—Fundamentals of Acoustics, Modelling, Simulation, Algorithms and Acoustic Virtual Reality*, 1st ed.; Springer: Berlin/Heidelberg, Germany, 2008. [CrossRef]
54. Torija, A.J.; Li, Z.; Chaitanya, P. Psychoacoustic modelling of rotor noise. *J. Acoust. Soc. Am.* **2022**, *151*, 1804–1815. [CrossRef]
55. Boucher, M.A.; Christian, A.W.; Krishnamurthy, S.; Tracy, T.; Begault, D.R.; Shepherd, K.; Rizzi, S.A. *Toward a Psychoacoustic Annoyance Model for Urban Air Mobility Vehicle Noise*; Technical Report Technical Memorandum 20240003202; NASA; Langley Research Center: Hampton, VA, USA, 2024. Available online: https://ntrs.nasa.gov/citations/20240003202 (accessed on 17 March 2026).
56. Rizzi, S.A.; Sahai, A.K. Auralization of air vehicle noise for community noise assessment. *CEAS Aeronaut. J.* **2019**, *10*, 313–334. [CrossRef]
57. Asmer, L.; Pak, H.; Prakasha, P.S.; Schuchardt, B.I.; Weiand, P.; Meller, F.; Torens, C.; Becker, D.; Zhu, C.; Schweiger, K.; et al. Urban air mobility use cases, missions and technology scenarios for the HorizonUAM project. In Proceedings of the AIAA Aviation 2021 Forum, Virtual Event, 2–6 August 2021; AIAA Paper 2021-3198. [CrossRef]
58. Shiva Prakasha, P.; Naeem, N.; Ratei, P.; Nagel, B. Aircraft architecture and fleet assessment framework for urban air mobility using a system of systems approach. *Aerosp. Sci. Technol.* **2022**, *125*, 107072. [CrossRef]
59. Ratei, P.; Naeem, N.; Prakasha, P.S. Development of an urban air mobility vehicle family concept by system of systems aircraft design and assessment. *J. Phys. Conf. Ser.* **2023**, *2526*, 012043. [CrossRef]
60. Ratei, P. Development of a Vertical Take-Off and Landing Aircraft Design Tool for the Application in a System of Systems Simulation Framework. Master's Thesis, Hamburg University of Applied Sciences (HAW Hamburg), Hamburg, Germany, 2022. Available online: https://elib.dlr.de/186947/ (accessed on 17 March 2026).

61. Gerhold, T. Overview of the Hybrid RANS Code TAU. In *MEGAFLOW—Numerical Flow Simulation for Aircraft Design, Notes on Numerical Fluid Mechanics and Multidisciplinary Design (NNFM)*; Kroll, N., Fassbender, J.K., Eds.; Springer: Berlin/Heidelberg, Germany, 2005; Volume 89, pp. 81–92.
62. Langer, S.; Schwoeppe, A.; Kroll, N. The DLR Flow Solver TAU—Status and Recent Algorithmic Developments. In Proceedings of the 52nd Aerospace Sciences Meeting, National Harbor, MD, USA, 13–17 January 2014; AIAA Paper 2014-0080. [CrossRef]
63. Staggat, M.; Ludowicy, J.; Bahrs, V.; Link, A.; Kazula, S. Modelling of a battery supported fuel cell electric power train topology for a regional aircraft. *J. Phys. Conf. Ser.* **2023**, *2526*, 012061. [CrossRef]
64. Ludowicy, J.; Bahrs, V.J.; Staggat, M. Feasibility study for a medium-range regional aircraft retrofit with battery powered propulsion system. In Proceedings of the Aerospace Europe Conference 2023—10th EUCASS—9th CEAS, Lausanne, Switzerland, 9–13 July 2023. [CrossRef]
65. Link, A.; Staggat, M. Characterisation of thermal management specific heat rejection for electric propulsion architectures. In Proceedings of the Aerospace Europe Conference 2023—10th EUCASS—9th CEAS, Lausanne, Switzerland, 9–13 July 2023. [CrossRef]
66. Bahrs, V.J.; Franke, F.; Kazula, S.; de Graaf, S. Analysis of the potential of metal hydride-based range extenders for electric commuter aircraft. *CEAS Aeronaut. J.* **2024**, *16*, 255–273. [CrossRef]
67. Ludowicy, J.; Ratei, P.; de Graaf, S. Comparison of energy sources for an electric powertrain in a tilt-rotor urban air mobility vehicle. *Eng. Proc.* **2025**, *90*, 69. [CrossRef]
68. Kalt, S.; Erhard, J.; Lienkamp, M. Electric machine design tool for permanent magnet synchronous machines and induction machines. *Machines* **2020**, *8*, 15. [CrossRef]
69. Teichert, E.; Kazula, S. Overview and Evaluation of Electric Machines for Electric Regional Aircraft Propulsion Systems. In Proceedings of the Deutscher Luft- und Raumfahrtkongress 2024, Deutsche Gesellschaft für Luft- und Raumfahrt—Lilienthal-Oberth e.V., Hamburg, Germany, 30 September–2 October 2024. [CrossRef]
70. Betz, A. Schraubenpropeller mit geringstem Energieverlust. *Rep. R. Soc. Sci. Gött. Math. Phys. Kl.* **1919**, *1919*, 193–217.
71. Goldstein, S. On the Vortex Theory of Screw Propellers. *Proc. R. Soc. Lond.* **1929**, *123*, 440–465. [CrossRef]
72. Helmbold, H.B. Der Entwurf einer Luftschraube für gegebene Betriebsverhältnisse. In *Ringbuch der Luftfahrttechnik*. 1937. Available online: https://www.deutsche-digitale-bibliothek.de/item/UC5IVTULLQIY7AT73S6KQ24H7UP3257O (accessed on 17 March 2026).
73. Larrabee, E. Practical Design of Minimum Induced Loss Propellers. *Bus. Aircr. Meet. Expo.* **1979**, *88*, 2053–2062. [CrossRef]
74. Adkins, C.N.; Liebeck, H.L. Design of Optimum Propellers. *J. Propuls. Power* **1994**, *10*, 676–682. [CrossRef]
75. Eppler, R.; Hepperle, M. A procedure for Propeller Design by Inverse Methods. In Proceedings of the International Conference on Inverse Design Concepts in Engineering Sciences (ICIDES), Washington, DC, USA, 23–25 October 1984; pp. 445–460.
76. Hepperle, M. Inverse Aerodynamic Design Procedure for Propellers Having a Prescribed Chord-Length Distribution. *J. Aircr.* **2010**, *47*, 1867–1871. [CrossRef]
77. Pott-Pollenske, M.; Delfs, J. Enhanced capabilities of the aeroacoustic wind tunnel Braunschweig. In Proceedings of the 14th AIAA/CEAS Aeroacoustics Conference (29th AIAA Aeroacoustics Conference), Vancouver, BC, Canada, 5–7 May 2008; AIAA Paper 2008-2910. [CrossRef]
78. Stuermer, A. Unsteady Euler and Navier-Stokes Simulations of Propellers with the Unstructured DLR TAU-Code. In *Proceedings of the New Results in Numerical and Experimental Fluid*; Mechanics, V., Rath, H.J., Holze, C., Heinemann, H.J., Henke, R., Hönlinger, H., Eds.; Springer: Berlin/Heidelberg, Germany, 2006; pp. 144–151. [CrossRef]
79. Roosenboom, E.W.M.; Stuermer, A.; Schroeder, A. Advanced Experimental and Numerical Validation and Analysis of Propeller Slipstream Flows. *J. Aircr.* **2010**, *47*, 284–291. [CrossRef]
80. Broszat, D.; Selic, T.; Marn, A. Verification of the Inverse Cut-off Effect in a Turbomachinery Stage—Part 1—Numerical results. In Proceedings of the 18th AIAA/CEAS Aeroacoustics Conference (33rd AIAA Aeroacoustics Conference), Colorado Springs, CO, USA, 4–6 June 2012; AIAA 2012-2306. [CrossRef]
81. Broszat, D.; Selic, T.; Marn, A. Verification of the Inverse Cut-off Effect in a Turbomachinery Stage—Part 2—Comparison to experimental results. In Proceedings of the 19th AIAA/CEAS Aeroacoustics Conference, Berlin, Germany, 27–29 May 2013; AIAA 2012-2306. [CrossRef]
82. Schade, S.; Jaron, R.; Moreau, A.; Guérin, S. Mechanisms to reduce the blade passing frequency tone for subsonic low-count OGV fans. *Aerosp. Sci. Technol.* **2022**, *125*, 107083. [CrossRef]
83. Duncan, P.E.; Dawson, B. Reduction of interaction tones from axial flow fans by suitable design of rotor configuration. *J. Sound Vib.* **1974**, *33*, 143–154. [CrossRef]
84. Tyler, J.M.; Sofrin, T.G. *Axial Flow Compressor Noise Studies*; Pre-1964 SAE Technical Papers; SAE International: Warrendale, PA, USA, 1962. [CrossRef]
85. Schade, S.; Jaron, R.; Klähn, L.; Moreau, A. Smart Blade Count Selection to Align Modal Propagation Angle with Stator Stagger Angle for Low-Noise Ducted Fan Designs. *Aerospace* **2024**, *11*, 259. [CrossRef]

86. Tapken, U.; Caldas, L.; Meyer, R.; Behn, M.; Klähn, L.; Jaron, R.; Rudolphi, A. Fan Test Rig for Detailed Investigation of Noise Generation Mechanisms due to Inflow Disturbances. In Proceedings of the AIAA AVIATION 2021 FORUM, Virtual Event, 2–6 August 2021. [CrossRef]
87. Moreau, A.; R., S.; Mennicken, M. Acoustic preliminary design of a low-noise fan stage considering a variable-area nozzle and variable-pitch rotor blades. *CEAS Aeronaut. J.* **2023**, *14*, 325–341. [CrossRef]
88. Schade, S.; Ludowicy, J.; Ratei, P.; Hepperle, M.; Stürmer, A.; Rossignol, K.S.; de Graaf, S.; Geyer, T.F. Conceptual Design of Electrically-Powered Urban Air Mobility Vehicles for Aeroacoustic Studies. In Proceedings of the Deutscher Luft- und Raumfahrtkongress, Hamburg, Germany, 30 September–2 October 2024.